Unpacking the drivers of diurnal dynamics of sun-induced chlorophyll fluorescence (SIF): Canopy structure, plant physiology, instrument configuration and retrieval methods

Authors:

Christine Y. Chang[1,2*], Jiaming Wen[2], Jimei Han[2], Oz Kira[2], Julie LeVonne[2], Longlong Yu[2^], Jeffrey Melkonian[2], Susan J. Riha[3], Ruiqing Zhou[2], Joseph Skovira[4], Cong Wang[2], Xu Shan[2], Yangyang Fan[2], Sharon Ng[2], Lianhong Gu[5], Jeffrey D. Wood[6], Paul Näthe[7], Ying Sun[2*]

Affiliations:

[1] USDA, Agricultural Research Service, Adaptive Cropping Systems Laboratory, Beltsville, MD, USA

[2] School of Integrative Plant Science, Soil and Crop Sciences Section, Cornell University, Ithaca, NY, USA

[3] Department of Atmospheric and Earth Sciences, Cornell University, Ithaca, NY, USA

[4] Department of Electrical and Computer Engineering, Cornell University, Ithaca, NY, USA

[5] Environmental Sciences Division and Climate Change Science Institute, Oak Ridge National Laboratory, Oak Ridge, TN, USA

[6] School of Natural Resources, University of Missouri, Columbia, MO, USA

[7] JB Hyperspectral Devices GmbH, Düsseldorf, Germany

[*] Corresponding authors. Email addresses: christine.chang@usda.gov; ys776@cornell.edu

[^] Present address: School of Resources and Environment, University of Electronic Science and Technology of China, Chengdu, Sichuan 611731, China

Keywords: sun-induced chlorophyll fluorescence (SIF), diurnal SIF dynamics, mechanistic SIF model, canopy structure, plant physiology, crop row orientation, SIF instrumentation, and SIF retrieval

Abstract

Sun-induced chlorophyll fluorescence (SIF) from spaceborne sensors is a promising tool for global carbon cycle monitoring, but its application is constrained by insufficient understanding of the drivers underlying diurnal SIF dynamics. SIF measurements from ground-based towers can reveal diurnal SIF dynamics across biomes and environmental conditions; however, meaningful interpretation of diurnal variations requires disentangling impacts from canopy structure, plant physiology, instrument configuration and retrieval methods, which often interact with and confound each other. This study aims to unpack these drivers using 1) concurrent ground and airborne canopy-scale and leaf-scale measurements at a corn field, 2) a mechanistic SIF model that explicitly considers the dynamics of photochemistry (via the fraction of open photosystem II reaction centers, qL) and photoprotection (via nonphotochemical quenching, NPQ) as well as their interactive dependence on the sub-canopy light environment, and 3) cross-comparison of SIF instrument configurations and retrieval methods. We found that crop row orientations and sun angles can introduce a distinctive midday dip in SIF in absence of stress, due to a midday drop of absorbed photosynthetically active radiation (APAR) when crop rows are north-south oriented. Canopy structure caused distinctive responses in both qL and NPQ at different positions within the vertical canopy that collectively influenced fluorescence quantum yield (Φ_F) at the leaf scale. Once integrated at the canopy scale, diurnal dynamics of both APAR and canopy escape probability (ε) are critical for accurately shaping diurnal SIF variations. While leaf-level qL and NPQ exhibited strong diurnal dynamics, their influence was attenuated at the canopy scale due to opposing effects on SIF at different canopy layers. Furthermore, different system configurations (i.e., bi-hemispherical vs. hemispherical-conical) and retrieval methods can bias the SIF magnitude and distort its diurnal shapes, therefore confounding the

interpretation of inherent strength and dynamics of SIF emission. Our findings demonstrate the importance of crop row structures, interactive variations in canopy structure and plant physiology, instrument configuration, and retrieval method in shaping the measured dynamics of diurnal SIF. This study highlights the necessity to account for these factors to accurately interpret satellite SIF, and informs future synthesis work with different SIF instrumentation and retrieval methods across sites.

1. Introduction

Accurate estimation of global photosynthesis or gross primary productivity (GPP) is critical for monitoring the global carbon cycle. These processes are highly sensitive to climate change and rising CO_2, yet existing process-based models are susceptible to prediction errors, partly because they are poorly constrained by reliable direct measurements at canopy scale and beyond (Anav et al., 2015; Beer et al., 2010). Sun-induced chlorophyll fluorescence (SIF) offers a promising solution to this limitation. SIF is the passive emission of light by chlorophyll molecules that absorb more light energy than can be used for photosynthesis or dissipated via non-photochemical quenching (NPQ) (Baker et al. 2008). It is a remotely detectable optical signal that contains direct functional information related to photosynthesis (Porcar-Castell et al. 2014).

There has been a rapid accumulation of SIF measurements from satellites (e.g., Frankenberg et al., 2011; Joiner et al., 2011; Köhler et al., 2020; Sun et al., 2018), ground-based towers (e.g., Campbell et al., 2019; Chang et al., 2020a; Dechant et al., 2020; Grossmann et al., 2018; Gu et al., 2019b; Li et al., 2020; Liu et al., 2017; Magney et al., 2019; Miao et al., 2018; Wieneke et al., 2018; Yang et al., 2018; Yang et al., 2015; Zhang et al., 2020) and airborne platforms (Atherton et al., 2016; Bendig et al., 2019; Cendrero-Mateo et al., 2019; Chang et al., 2020b; Colombo et al., 2018; Frankenberg et al., 2018; Rascher et al., 2015; Siegmann et al., 2019; Wang et al., 2021; Wieneke et al., 2016). Early studies identified a consistent linear relationship between satellite SIF and canopy GPP across biomes at the seasonal scale (Sun et al. 2017, Li et al. 2018). The reported linearity was interpreted with the light use efficiency (LUE) based SIF-GPP formulations, defined as:

$$GPP = LUE_P \times PAR \times fPAR \qquad \text{(Monteith 1972)} \qquad (1a)$$

$$SIF = LUE_F \times PAR \times fPAR \times \varepsilon \quad \text{(Porcar-Castell et al. 2014)} \quad (1b)$$

where LUE_P represents the light use efficiency of photosynthesis (CO_2 fixed per unit of absorbed light); LUE_F represents the light use efficiency of chlorophyll fluorescence (fluorescence produced per unit of absorbed light); PAR represents the amount of incident photosynthetically active radiation; fPAR represents the fraction of PAR absorbed by vegetation; and ε represents the probability for total emitted fluorescence photons to escape from the canopy. From these LUE-type formulae, we can see that both SIF and GPP share absorbed PAR (APAR, i.e., fPAR × PAR) as a common driver, which predominantly explains the previously identified SIF-GPP linearity at seasonal scales or beyond or coarse spatial resolutions (Yang et al., 2015).

A growing number of studies demonstrate a nonlinear SIF-GPP relationship at finer spatial/temporal scales or under stress (Campbell et al., 2019; Damm et al., 2010; He et al., 2020; Li et al., 2020; Magney et al., 2020; Marrs et al., 2020; Tagliabue et al., 2019). Unlike reflectance or vegetation indices, which are relatively stable over short timespans, SIF fluctuates instantaneously with PAR and dynamic regulations of photosynthesis and NPQ (Porcar-Castell et al., 2014). Existing satellites with SIF capabilities record discretely during an overpass, requiring scaling of these instantaneous SIF measurements to daily values in order to match GPP; this is usually based on a simplified harmonic diurnal variation of solar radiation (Frankenberg et al., 2011; Hu et al., 2018; Sun et al., 2018). Consequently, a mechanistic understanding of diurnal SIF dynamics and its underlying drivers is critical for accurately upscaling and interpreting satellite SIF measurements as well as its dynamic relationships with photosynthesis (e.g., Campbell et al., 2019; Miao et al., 2018, 2020; Xu et al., 2018; Yang et al., 2018).

At the diurnal scale, APAR should be the dominant driver of SIF at the canopy scale (Dechant et al., 2020; Miao et al., 2018, 2020; Yang et al., 2018). However, recent leaf-level studies have also reported important regulations from physiology, particularly the competing influences of NPQ and photosynthesis on SIF yield at short time scales and under stress (Acebron et al., 2021; Marrs et al., 2020). Reconciling these discrepancies requires a mechanistic model that can guide the interpretation of underlying drivers. To date, attempts to do so have relied upon simple statistical regressions of components of the LUE model; although useful as initial exploration, such approaches are susceptible to measurement noise and do not disentangle the contributions of plant physiology from other factors (e.g., canopy structure). Critically, the LUE-type model (Eq. 1b) masks considerable complexity of physiological processes and their interaction with canopy structural variations, making the interpretation of LUE_F variations and its linkage with NPQ dynamics elusive (Gu et al., 2019a).

Additional complexity in diurnal SIF dynamics can arise from non-homogeneous canopies, which can create a highly dynamic light environment that influences photosynthesis and NPQ within the canopy (Niinemets, 2010; Palmer, 1989; Stewart et al., 2003; Lappi & Stenberg, 1998; Sinoquet & Bonhomme, 1992) and hence SIF emission. For example, at certain solar angles, shaded leaves may be suddenly exposed to higher light intensities, e.g., sunflecks, causing more photosystem II (PSII) reaction centers to be occupied (i.e., decreases in qL, which represents the fraction of open PSII reaction centers) while NPQ concomitantly increases to offset the absorption of excess light energy. As a result, canopy structure, plant physiology, and solar geometry interactively impact the emission of SIF, and such interaction depends on canopy architectures. Specifically, agricultural fields planted with row crops exhibit a distinctive regular architecture; their canopy light interception is influenced by row spacing, orientation and plant

98 traits (Awal et al., 2006; Maddonni et al., 2001; Stewart et al., 2003). Previous work by Zhao et
99 al. (2016) investigated the impact of row structures on SIF emission through modeling and field
100 measurements. By comparing row structures with homogeneous canopies, Zhao et al. suggested
101 that row structure has a large impact on SIF magnitude and directionality. If this is the case, we
102 may logically extrapolate that when satellite SIF is used for large-scale agriculture monitoring, it
103 may be influenced by crop row structures that could potentially impact the estimation of daily
104 SIF from instantaneous soundings.

105 Furthermore, when working with ground SIF observations, it is important to address potential
106 confounding factors, to avoid erroneously attributing biological significance to measurements
107 noise from system configurations and retrieval methods. For example, SIF retrieval methods
108 using the far-red telluric oxygen (O_2A) band can greatly differ in SIF magnitude under cloudy
109 and clear conditions (Chang et al., 2020a). Moreover, this effect, which manifested as distortion
110 of the edges of the O_2A band, differed between system configurations with hemispherical vs.
111 conical acquisition of upwelling radiance (Chang et al., 2020a). Despite the important
112 implications of such effects, the confounding factors from system configuration and retrievals
113 have not been explicitly considered in previous studies that examined the drivers of diurnal SIF
114 dynamics.

115 In this study, we seek to understand the factors that control the diurnal dynamics of SIF
116 retrieved at the canopy scale using ground-based tower systems. These include the biological
117 factors (canopy structure and plant physiology) that determine the inherent strength of SIF
118 emission, and the physical acquisition of SIF from the canopy, influenced by the instrument
119 system configuration and retrieval methods. Specifically, we aim to address: 1) How do canopy
120 structure (APAR and ε) and plant physiology (NPQ and qL) interactively influence the diurnal

SIF dynamics? 2) To what extent can highly structured canopies (such as agricultural row structures) impact diurnal SIF dynamics? 3) How do systematic errors introduced by system configuration and retrieval methods confound the interpretation of biophysical processes driving SIF dynamics? Answering these questions is necessary for correctly attributing biological factors that determine the diurnal cycle of SIF, ensuring the accuracy of upscaling satellite SIF from instantaneous to daily integrals, and informing future synthesis work with different SIF instrumentation and retrieval methods across sites.

To achieve these objectives, we first utilized a mechanistic SIF model (Gu et al., 2019a; section 2.3) that explicitly considers the NPQ and qL dynamics as well as their interactive dependence on canopy-structure regulated sub-canopy light environment to understand the diurnal SIF patterns as well as the underlying drivers. Here we leveraged the unique canopy architecture of corn row crops, which provide ideal targets for exploring the interactive influence of canopy structure, plant physiology, and solar geometry on SIF dynamics. Second, we performed diurnal canopy-level SIF measurements with ground and UAV instruments as well as diurnal leaf-level chlorophyll fluorescence (ChlF) measurements for corn fields with contrasting row orientations, to assess the extent to which highly structured canopies, as opposed to horizontally more homogeneous canopies (i.e., broadleaf forests or grasslands), impact diurnal SIF dynamics. Lastly, we compared the clear-day diurnal SIF patterns retrieved by two hemispherical (FAME) and two conical (FloX) system configurations over four different vegetation types, to determine whether there are artificial influences on the diurnal shape of SIF which may be introduced by instrument setup and/or retrieval methods.

2. Methods

Here we describe SIF instrument configurations and field sites (section 2.1); canopy-level SIF acquired with ground and UAV platforms (section 2.2); chlorophyll fluorescence acquired at the leaf level (section 2.3); and mechanistic SIF modeling (section 2.4). An overview of the measurements, site characteristics, and the associated research questions is described in Table 1.

Table 1. Overview of measurements and sites used in this study. Sites include Cornell Musgrave Research Farm (CMRF), Missouri Ozark AmeriFlux (MOFLUX), Grossetto Italy (GROS) and Jülich Germany (JULI). Sites and platforms are described in Section 2.1.

Research Questions	Sites	Platform	Measurements
How do agricultural row structures impact SIF emission?	CMRF	FAME-1	Canopy APAR, SIF, NDVI, ρ_{NIR}, NIR_V
	CMRF	FAME-1-UAV	Canopy SIF
How do they influence canopy structure and plant physiology?	CMRF	GFS-3000	Leaf-level chlorophyll fluorescence
	MOFLUX	FAME-2	Canopy APAR, SIF
What confounding impacts from instrumentation and retrieval methods influence the detected SIF signal?	CMRF	FAME-1	Canopy SIF
	MOFLUX	FAME-2	Canopy SIF
	GROS	FloX-1	Canopy SIF
	JULI	FloX-2	Canopy SIF

2.1 Description of tower SIF systems and field site characteristics

Concurrent SIF and hyperspectral reflectance measurements were collected at four stationary tower sites with different canopies and instrument configurations (Table 2). The two configurations include a bi-hemispherical system, i.e. ~180° FOV collection of both upwelling and downwelling irradiance, and a hemispherical-conical system, i.e. ~180° FOV for downwelling but a narrower FOV (here, 25°) for upwelling radiance. The FAME bi-hemispherical system (Gu et al., 2019b) was deployed at Cornell Musgrave Research Farm (denoted as FAME-1) and the Missouri Ozark AmeriFlux site (FAME-2), while the commercial hemispherical-conical FloX system (Julitta et al., 2016) was deployed at Grossetto, Italy (FloX-1) and Jülich, Germany (FloX-2). All four systems were positioned over the target canopies with

a nadir viewing zenith angle. A description of the system specification is shown in Table 2, and climate and vegetation type information for the four sites used in this study is shown in Table 3.

Table 2. Comparison of SIF systems. Bi-hemi denotes bi-hemispherical FOV configuration (downwelling and upwelling both 180°). Hemi-con denotes hemispherical-conical FOV configuration (downwelling ~180°, upwelling narrower FOV). Note that the 180° FOV listed for all instruments are in reality closer to 160° in implementation due to manufacturing design of the cosine corrector (Gu et al. 2019a), while ~85-92% of light is acquired within 100° (Chang et al., 2020b).

Instrument	**Config.**	**Spectral range (nm)**	**Spectral resolution (nm FWHM)**	**Spectral sampling interval (nm)**	**Signal-to-Noise Ratio**	**Upwelling Field-of-View**
FAME	Bi-hemi	730-784	~0.15	~0.05	1000:1	~100°
FloX	Hemi-con	640-800	~0.30	~0.17	1000:1	~25°

Table 3. Description of sites used in this study. Meteorological data presented here are historical mean climatology of 1981-2010, which were obtained from NOAA (https://www.ncdc.noaa.gov/cdo-web/) for CMRF and MOFLUX, and from Julich climate station (https://www.fz-juelich.de/gs/DE/UeberUns/Organisation/S-U/Meteorologie/klima/statistik_node.html) and meteostat (https://meteostat.net/en/) for GROS. For the purposes of footprint calculation, we use 100° FOV to calculate the effective footprint diameter of the FAME systems.

Instrument	Years	Site	Vegetation type	Average annual precip. (mm)	Average annual temp. (°C)	Sensor height above canopy (m)	Footprint diameter (m)
FAME-1	2018-2019	CMRF	Corn	918	9.2	~1.5-2	~4.6
FAME-1-UAV	2019	CMRF	Corn	918	9.2	10	~23.8
FAME-2	2017	MOFLUX	Deciduous forest	1176	13.3	~13.5	~32.2
FloX-1	2018	GROS	Alfalfa	749	16.0	~1.5	~0.7
FloX -2	2018	JULI	Grass	718	10.5	~3	~1.3

2.1.1 FAME

The core of the FAME tower system consists of a thermally stabilized hyperspectral spectrometer (QE-Pro, Ocean Optics Inc., Dunedin, FL, USA) configured for far-red SIF

retrieval (730-784 nm), maintained in a temperature-regulated enclosure and connected to an armored and weatherproofed fiber optic equipped with an opaline glass cosine corrector (CC-3, Ocean Optics Inc.) which rotates between zenith and nadir positions using an external motor. In this manner, the system alternates between sampling hemispherical upwelling and downwelling radiation. Further system details are provided in Chang et al. (2020a) and Gu et al. (2019b).

2.1.2 FAME-1: Cornell Musgrave Research Farm, USA

FAME-1 was deployed at Cornell Musgrave Research Farm (CMRF), an agricultural site located in upstate New York (42° 43′ 22″ N, 76° 39′ 46″ W). The field, measured 520 m × 290 m, was planted with a commercial corn hybrid in 2018 and 2019 using 76 cm spacing between rows, 15.25 cm spacing within row, and a north-south (N-S) row orientation to minimize soil erosion. For further site details, see (Chang et al., 2020a). In 2019, in addition to the first field where FAME-1 was deployed, a second field consisting of five 10 m x 10 m plots was planted nearby with the same hybrid, planting density and row spacing but with east-west (E-W) row orientation.

In addition to SIF, the FAME-1 tower system was equipped with a second hyperspectral spectrometer (FLAME, Ocean Optics Inc.) for broadband reflectance (400-950 nm), with a spectral resolution of 1.3 nm FWHM and SNR of 250:1. Both QE Pro and FLAME spectrometers were connected to the same cosine-corrected fore-optic for collecting light using a single-bifurcated fiber optic. FAME-1 utilized two dataloggers (CR1000, Campbell Scientific, Logan, UT, USA) to record meteorological measurements including temperature and relative humidity (CS215, Campbell Scientific), barometric pressure (CS106 PTB110, Vaisala, Helsinki, Finland), PAR (PQS1, Kipp & Zonen B.V., Delft, the Netherlands), and APAR using a series of line quantum sensors (SQ311, Apogee Instruments, Logan, UT, USA). The meteorological

measurements were acquired at the same frequency as downwelling irradiance from the SIF and hyperspectral spectrometers.

A smaller, lightweight version of the FAME-1 system, comprised of similar spectrometer configurations, was deployed on a UAV (herein referred to as FAME-1-UAV) to enable monitoring of the two corn fields with contrasting row orientation in 2019. This system is described in Chang et al., (2020b).

2.1.3 FAME-2: Missouri Ozark AmeriFlux site, USA

FAME-2 was deployed at the MOFLUX site (38° 44′ 39 ″N, 92° 12′ 00″ W), a second-growth deciduous forest site of the oak-hickory (*Quercus-Carya*) type in central Missouri. For field site details, including species descriptions, see Gu et al. (2016). In addition to SIF, the FAME-2 tower system utilized a datalogger (CR6, Campbell Scientific) to record meteorological measurements including temperature and relative humidity (CS215, Campbell Scientific) and PAR (PQS1, Kipp & Zonen). The meteorological measurements are acquired at the same frequency as downwelling irradiance.

2.1.4 FloX

The FloX system consists of one thermally stabilized hyperspectral spectrometer (QE-Pro) configured for red to far-red SIF retrieval (650-800 nm) and a second hyperspectral spectrometer (FLAME) for broadband reflectance (400-950 nm). Both non-imaging spectrometers are maintained in a temperature-regulated compartment and connected via a bifurcated fiber optic to an optical shutter, which switches sampled light between fixed upwelling and downwelling channels. The down-welling light is measured through a cosine diffusor while the up-welling light is measured through fiber optics with 25° FOV. The system is designed to function fully

autonomously in the field and stores data on an internal SD card. Further details are provided in Julitta et al., (2016) and Burkart et al., (2015).

2.1.5 FloX-1: Grossetto, Italy

FloX-1 was deployed in Grossetto (GROS), central Tuscany, Italy (42°49′41″N, 11°04′08″E). The site is characterized as a segmented agricultural area with various crops. A solar-powered FloX was installed over a mature, closed canopy of alfalfa. The instrument was installed with a few meters distance to canopy to allow for recording a reasonable area of recording (ca. 1.0 m²) in a uniform and closed canopy while minimizing influences of atmospheric distortion. The site was also used periodically for airborne measurement campaigns in 2018 during the ESA-funded FleXsense campaign. For further site details, see Cogliati et al. (2019).

2.1.6 FloX-2: Jülich, Germany

FloX-2 was deployed at the Research Center Jülich (JULI), in Jülich, Germany (50°54′36″N 6°24′50″E) on a grass lawn in front of the institute IBG-2 Plant Sciences. The Jülich weather station is in close proximity to the Research Center, and provides a comprehensive record of weather data, irradiance measurements, cloud cover, aerosols, emission and fluxes on a 124 m high tower. The FloX was installed within a few meters' distance of the tower to record a field of view of ca. 1.5 m² over a uniform and closed canopy. The grass was initially mowed before the instrument was installed and then left to grow naturally during the spring growth period, reaching a closed, fully developed canopy in May.

2.2 Canopy-level measurements of SIF

2.2.1 Tower-based diurnal measurements of canopy SIF

Measurements by all SIF towers were performed continuously during daylight hours with the integration time of each measurement optimized to maximize spectrometer dynamic range. The FAME-1 dataset used in this study included clear-sky measurements collected over the peak growing seasons in 2018 (DOY 200-250) and 2019 (DOY 215-250) from the same corn field at CMRF; planting occurred on DOY 145 in 2018 and 158 in 2019. The FAME-2 dataset used in this study included eleven clear-sky days ranging from DOY 126 to 176 collected in 2017 from the natural deciduous forest at MOFLUX. The FloX-1 dataset used in this study included six clear days ranging from DOY 97 to 115 collected over mature alfalfa at GROS in 2018; planting occurred on DOY 51. The FloX-2 dataset used in this study included twelve clear days ranging from DOY 96 to 129 collected over a fully developed and closed grass canopy at JULI in 2018.

2.2.2 UAV-based diurnal measurements of canopy SIF

Measurement campaigns using FAME-1-UAV were performed at CMRF over two clear days in 2019 across the peak and late growing seasons, consisting of one day in the N-S oriented field and one day in the E-W oriented field. During each campaign, flights were performed hourly from 9:00 h to 18:00 h (flights before 9:00 h were not possible due to mist and high humidity impacts on the performance of the spectrometers). Each flight mission consisted of six stop-and-go waypoints over the N-S field or five waypoints over the E-W field (for more details see Chang et al., 2020b). Flight altitude was 12 m to maintain a minimum of 10 m over the crop canopy, to avoid impacts of downdrafts from the drone on the canopy during measurement. Because the payload containing the spectrometers was not thermally regulated, radiometric calibrations and dark-current curves were performed immediately before or after each flight.

2.2.3 SIF retrieval and quality control

For the purposes of this study, only clear days were used for analysis. This decision was based on our prior study in which we identified that clouds not only decrease SIF magnitude but could distort SIF retrieval (Chang et al., 2020a). Additionally, the inconsistency of clouds appearing during the day would complicate discussion of canopy structural effects on light interception. Identification of clear days was performed by calculating the clearness index, following Chang et al. (2020a).

Our choice of SIF retrieval method was constrained by the instrument systems used in this study. We focused our analysis on far-red SIF as the FAME systems are configured for far-red SIF retrieval only (Table 2), although red SIF, a signal additionally complicated by canopy re-absorption, is certainly deserving of further investigation. Furthermore, telluric SIF retrievals from the O_2A band are known to be susceptible to distortion at the edges of the O_2A well, which is avoided by retrieving SIF from solar Fraunhofer lines (Chang et al., 2020a). However, due to the lower spectral resolution of the FloX systems and the high noise known to affect Fraunhofer retrievals even from the FAME systems (Chang et al., 2020a), we chose to utilize O_2A rather than Fraunhofer retrievals. Thus, SIF was retrieved from the O_2A band via the spectral fitting method (SFM) using both the traditional wide (759-767.76 nm, denoted as SFM_{wide}) and adjusted narrow (759.5-761.5 nm for FAME, 758-764 nm for FloX, denoted as SFM_{narrow}) fitting windows according to Chang et al. (2020a). The adjusted fitting window used for FloX was slightly wider than that for FAME due to the lower spectral resolution of the QE Pro spectrometer used in the FloX system. For FAME-1-UAV, SIF was retrieved using SFM_{narrow}.

Quality control was applied to all systems as follows: Measurements were only used if they satisfied the criteria of $< 70°$ solar zenith angle (SZA), sufficient goodness-of-fit ($0.5 < \chi^2 < 2$), where χ^2 is the reduced χ^2 of the retrieval residuals. Furthermore, to avoid complication of the

result by atmospheric impacts, we only examined clear days where clearness index (CI), defined as the ratio of actual to potential PAR, was between 0.9 and 1. More details on the screening procedure are described in Chang et al. (2020a).

FloX measurements were filtered with the internal quality flags from the processing GUI. Following Cogliati et al. (2015), measurements were excluded where the detector was saturated, SZA > 70° and the relative difference between downwelling radiance measured at 750 nm just prior and just after a given upwelling measurement was < 1%, to screen out measurements recorded under unstable sky conditions.

2.3 Leaf-level measurements of chlorophyll fluorescence

Leaf-level chlorophyll fluorescence was measured at the FAME-1 site using a portable photosynthesis system (GFS-3000, Heinz Walz GmbH, Effeltrich, Germany) equipped with a pulse-amplitude-modulated (PAM) fluorescence measuring head (3056-FL, Walz). All leaf-level measurements were performed using set cuvette conditions of 25°C, 400 ppm CO_2 and 50-60% relative humidity. Diurnal measurements were collected during clear days in 2018 and 2019. Measurements were made in the N-S row-oriented field, adjacent to the deployment location of FAME-1, in 2018 (DOY 223, 227, 236, 267) and 2019 (DOY 241, 248). In 2019, measurements were also taken in a nearby E-W row-oriented field (DOY 217, 261).

For each of these measurement campaigns, pre-dawn measurements were first obtained on 5-6 healthy, mature leaves at the top of the canopy (unshaded leaves at ~1.5-2 m above ground) and 5-6 healthy, mature leaves at mid-canopy (ear leaf position, approximately 1 m above ground) to record maximal dark-adapted fluorescence (F_m) and basal dark-adapted fluorescence (F_o). Saturating pulses for F_m and maximal light-adapted fluorescence (F_m') measurements were

set at ~8,000 μmol m^{-2} s^{-1} for 0.6 seconds. All subsequent measurements were made at the same location on each leaf. Starting around 8:00 h local time, light-adapted fluorescence measurements were performed at ~40-60 minute intervals, positioning the cuvette parallel to the ground but carefully avoiding mechanical strain on each measured leaf. The actinic light applied during each light-adapted PAM measurement was determined by the actual PAR sensed at each position by the sensor attached to the measuring head. Measurements of steady-state fluorescence (F_s) and F_m' were recorded approximately 2-3 minutes after the leaf was inserted to the cuvette. Chlorophyll fluorescence parameters were then calculated as follows:

$\Phi_{PSII} = (F_m' - F_s)/F_m'$ (Genty et al., 1989) (2a)

$\Phi_{PSIImax} = (F_m - F_o)/F_m$ (Genty et al., 1989) (2b)

$\Phi_{NPQ} = (F_s/F_m') - (F_s/F_m)$ (Hendrickson et al., 2004) (2c)

$\Phi_{f,D} = F_s/F_m$ (Hendrickson et al., 2004) (2d)

$\Phi_D = \Phi_{f,D} - \Phi_F$ (Hendrickson et al., 2004) (2e)

$\Phi_F = \frac{1-\Phi_{PSIImax}}{(1+k_{DF})\times[(1+NPQ)\times(1-\Phi_{PSIImax})+q_L\times\Phi_{PSIImax}]}$ (Gu et al., 2019a) (2f)

$qL = (F_m' - F_s)/(F_m' - F_o') * (F_o'/F_s)$ (Kramer et al., 2004) (2g)

$NPQ = (F_m - F_m')/F_m'$ (Kramer et al., 2004) (2h)

Here Φ_{PSII} represents the effective quantum yield of PSII; $\Phi_{PSIImax}$ represents the maximum quantum yield of PSII; Φ_{NPQ} represents the quantum yield of nonphotochemical quenching (regulated heat dissipation), NPQ; $\Phi_{f,D}$ represents fraction of energy constitutively dissipated as heat or emitted as fluorescence; Φ_D represents the quantum yield of constitutive heat dissipation; Φ_F represents the quantum yield of chlorophyll fluorescence at the leaf level; qL represents the fraction of open PSII reaction centers under the lake connectivity of photosynthetic units (Kramer et al., 2004).

To realistically model the physiological response to diurnal changes in the light environment within a complex canopy (detailed in section 2.4.3), we needed to estimate NPQ and qL at different light intensities. Thus, we collected photosynthetic light response curves from six top-of-canopy (sunlit) and six mid-canopy (some sunlit, some shaded) mature, healthy corn leaves in 2018 (Fig. S2). Leaves were fully dark-adapted for a minimum of 30 minutes before F_m and F_o were acquired. The leaves were then exposed to a sequence of eight steps with increasing actinic light intensity (100, 200, 400, 800, 1200, 1800, 2500 μmol quanta m^{-2} s^{-1}) for 7-10 minutes per step. At each light intensity, F_s, F_o' and F_m' were acquired. Following Kramer et al. (2004), qL and NPQ were then calculated using Eqs. 2g,h.

2.4 A mechanistic model to estimate SIF and mechanistically attribute underlying drivers

In this study, we employed a mechanistic model to compute leaf-level SIF (Gu et al., 2019a) that explicitly considers the NPQ and qL. We decided to use this model because we can utilize real-time APAR to constrain the model, which is a considerably more parsimonious approach than a complex 3D radiative transfer model such as DART for simulating SIF. We did not use SCOPE to simulate SIF in this study, because 1) it is a 1D model that cannot adequately characterize 3D row structures or orientations, and 2) it derives fluorescence from simulated photosynthesis and NPQ, which can carry uncertainties from assumptions of inputs or parameters; such uncertainties have previously been shown to propagate into SIF estimations (Parazoo et al., 2019; Yang et al., 2021). The mechanistic approach employed here enables an in-depth analysis of how diurnal NPQ and qL dynamics affect SIF emissions, without concerning the potential uncertainties propagated from the photosynthesis or NPQ parameterizations. The leaf-level SIF was then integrated to the total canopy-level emission using the multi-layer approach, which was further converted to the at-sensor SIF observations using the parsimonious

escape probability formulation ε (Zeng et al., 2019). Collectively, the canopy-level SIF simulation is formulated as:

$$SIF = \varepsilon \times \sum_{L=0}^{LAI} (\Phi_{F,L} \times APAR_L) \times \beta \quad (3)$$

Here we use $\Phi_{F,L}$ (calculated via Eq. 2f) to represent the leaf-level quantum yield of chlorophyll fluorescence at layer L; β represents the fraction of absorbed light energy directed to PSII. Unit conversion was then performed according to Text S2 to match that of measured SIF retrieved at 760nm. From Eqs. 2f and 3, components related to plant physiology ($\Phi_{PSIImax}$, qL, NPQ) as well as canopy structure (ε, fPAR), in addition to the environmental driver PAR, influence SIF emission. Furthermore, these physiological terms are influenced by environmental conditions such as temperature and water availability, suggesting that these physiological responses are critical components of SIF (Marrs et al., 2020). The mechanistic SIF model (described in Eqs. 2f and 3) thereby provides a clear advantage over the traditional LUE model (Eq. 1) due to its explicit representation of physiological processes. Moreover, it accounts for interactions between physiology (represented by $\Phi_{PSIImax}$, qL, NPQ) and canopy structural variations (represented by APAR and ε), that modulate within-canopy light conditions, which are all hidden in the LUE_F term.

SIF simulations were performed using the FAME-1 (CMRF) dataset only, due to the lack of APAR, reflectance and leaf level physiological measurements needed to derive the model input factors in the other three sites. Continuous instantaneous measurements used as inputs to these simulations were recorded over three clear days (DOY 214, 217 and 238) in 2019, with detailed descriptions of each component (either direct measurements or derived from direct measurements) below.

383 *2.4.1 APAR measurements*

384 Canopy APAR was measured at CMRF during the 2019 growing season concurrently with
385 SIF measurements. APAR measurements at MOFLUX were only available from 2018 and 2019
386 as quantum line sensors were not yet installed in 2017, while APAR measurements were not
387 available from GROS or JULI. APAR was calculated according to Gitelson & Gamon (2015):

388 $$APAR = PAR_{in} - PAR_{out} - PAR_{transm} + PAR_{soil} \quad (4a)$$

389 $$fPAR = APAR / PAR_{in} \quad (4b)$$

390 where PAR_{in} represents the incident PAR at the top of the canopy; PAR_{out} represents the PAR
391 reflected by the vegetation, measured at the top of the canopy; PAR_{transm} represents the PAR
392 transmitted through the canopy; PAR_{soil} represents the PAR reflected by the soil, measured at the
393 bottom of the canopy.

394 At CMRF, PAR_{in} and PAR_{out} were each measured by a single line quantum sensor (SQ311,
395 Apogee Instruments) positioned approximately 1 m above the mature canopy. The SQ311 line
396 quantum sensors consist of a series of ten-point photodiode sensors covering 70 cm length.
397 PAR_{soil} was measured by a single downward-facing SQ311 line sensor positioned across a row,
398 approximately 5 cm above the soil surface. PAR_{transm} was calculated as the average of readings
399 from five upward-facing SQ311 line sensors positioned in series across a total of four rows,
400 positioned approximately 6 cm above the soil surface. At MOFLUX, PAR_{in} and PAR_{out} were
401 each measured by a single line sensor (SQ311, Apogee Instruments) positioned approximately
402 10 m above the mature canopy. PAR_{transm} and PAR_{soil} were measured at two different locations
403 within the trunk-space using upward and downward facing line quantum sensors.

404 *2.4.2 Estimation of canopy escape probability of SIF (ε)*

Hyperspectral reflectance was measured using the FAME-1 deployed at CMRF and used to derive the canopy escape probability of SIF (ε) following Zeng et al. (2019), using the APAR measurements (described in 2.3.1) in combination with NIRv:

$$NDVI = \frac{\rho_{NIR}-\rho_{red}}{\rho_{NIR}+\rho_{red}} \quad (5a)$$

$$NIR_V = NDVI \times \rho_{NIR} \quad (5b)$$

$$\varepsilon \approx \frac{NIR_V}{fPAR} \quad (5c)$$

where ρ_{NIR} and ρ_{red} were the reflectance values at 858 nm and 648 nm, respectively, based on wavelengths used to calculate NDVI from MODIS; NDVI is the normalized difference vegetation index; and NIR_V is the near-infrared reflectance of vegetation.

2.4.3 Calculation of sub-canopy qL, NPQ, and SIF quantum yield (Φ_F)

We employed a multi-layer strategy to compute the total SIF emission, prior to multiplication with ε (as formulated in Eq. 3). For each given layer L, we first computed incident PAR_L and $APAR_L$ as follows, constrained by actual measurements of canopy APAR and PAR_{in} (section 2.3.1):

$$APAR_L = APAR \times \frac{e^{-k\cdot L}(1-e^{-k\cdot dL})}{1-e^{-k\cdot LAI}} \quad (6a)$$

$$PAR_L = PAR_{in} \times e^{-k\cdot L} \quad (6b)$$

Here the total canopy LAI at peak season approximated to be 4. We then divided our corn canopy into eight layers, ranging from 0 to 3.5 with 0.5 canopy optical depth per layer. k denotes the extinction coefficient according to Beer's law, dynamically computed for each time step constrained by APAR measurements, as follows:

$$k = -\frac{\log\left(1-\frac{APAR}{PAR_{in}}\right)}{LAI} \quad (7)$$

Note the extinction coefficient k is diurnally varying with solar elevation angle. Using actual APAR measurements to constrain k can effectively account for the effect of highly structured canopy due to row spacing. The use of actual APAR measurements (here aggregated to 5-minute intervals) also implicitly corrects for uncertainty in the approximate LAI used in equations 6-7. The detailed derivation of Eqs. 6-7 is provided in Text S1.

Next, we computed instantaneous qL and NPQ for each layer, which in turn were used to calculate the corresponding $\Phi_{F,L}$. To achieve this, we employed empirical light response formulae to model qL and NPQ as a function of incident PAR at each layer, i.e., PAR_L. This approach allowed us to generate instantaneous qL and NPQ that changed across the day within each layer.

For qL at each layer (qL_L), we used a parsimonious exponential model:

$$qL_L = a \times e^{b \times PAR_L} + c \quad (8)$$

Here *a*, *b* and *c* are empirical coefficients.

For NPQ at each layer (NPQ_L), we used the model developed by Serôdio & Lavaud (2011):

$$NPQ_L = NPQ_{max} \times \frac{{PAR_L}^n}{{PAR_{50}}^n + {PAR_L}^n} \quad (9)$$

where NPQ_{max} represents the maximum NPQ value; PAR_{50} represents the light intensity required to activate half of the maximum NPQ; n is an empirical coefficient. Empirical coefficients for Eqs. 8-9, i.e., *a*, *b* and *c* for calculating qL, and PAR_{50} and *n* for calculating NPQ, were determined by fitting with leaf-level light response curve measurements collected across top and mid canopy leaves (section 2.3, Fig. S2).

Lastly, utilizing Eq. 3, $\Phi_{F,L}$ was computed using NPQ_L and qL_L. $\Phi_{PSIImax}$ was held at a constant value of 0.83 (Björkman & Demmig, 1987); β was assumed 0.4 for C4 plants (Yin & Struik, 2012). k_{DF} was assumed to be a constant value of 15, which was slightly adjusted from previously published value of 19 (Gu et al., 2019a; van der Tol et al., 2014) to match the magnitude of simulated total canopy SIF with measured SIF.

2.3.4 Scenario simulations

Using Eqs. 2f and 3, three scenario simulations were constructed to demonstrate the combined and individual contributions of canopy structure, plant physiology, and environmental drivers to the collective signal of SIF, as shown in Table 4. Where the factor was being tested, instantaneous data was simulated across layers using inputs derived from direct canopy-scale measurements taken at CMRF. Where the factor was not being tested, it was set to a constant value representing the average across time for each layer (for $\Phi_{F,L}$) or across time at the canopy scale (ε).

Table 4. Simulation scenarios testing the canopy structural, plant physiological, and environmental factors that control SIF dynamics.

Factor type	Instantaneous input	Constants
Canopy absorption + escape + physiology	$APAR_L$, ε, $\Phi_{F,L}$	-
Canopy absorption + escape	$APAR_L$, ε	$\Phi_{F,L}$
Canopy absorption only	$APAR_L$	ε, $\Phi_{F,L}$

3. Results

3.1 Diurnal SIF dynamics and its dependence on agricultural row orientations

We observed a midday dip in canopy SIF exhibited in the field with a north-south (N-S) row orientation, consistently from both tower and UAV platforms (Fig. 1). However, such pattern was absent in the field with east-west row orientation (E-W) (Fig. 1b), even though it was

planted with the same variety of corn and row spacing and developed under the same meteorological conditions as the N-S field. Such contrast indicates that agricultural row orientations can strongly impact the diurnal dynamics of SIF observations. When row crops such as corn are oriented more perpendicular to the trajectory of the sun (e.g., N-S), larger diurnal changes have been reported in the proportion of light intercepted by crops and soil, in comparison with row orientation more parallel to the trajectory of the sun (e.g., E-W) (Tsubo et al., 2001). This row structural effect could introduce a sudden drop in canopy light absorption while more light penetrates to soil in N-S planted corn fields (such as that measured at CMRF, Fig. 2a) when the solar zenith angle aligns with the row at midday, which in turn can result in a midday dip in SIF emission. This should also result in exposure of leaves positioned lower within the canopy to higher light intensities at such solar angles, as we explore below. The difference in magnitude of tower and UAV SIF in the N-S field was due to within-field heterogeneity between the positions measured by tower and UAV, as described in Chang et al. (2020b).

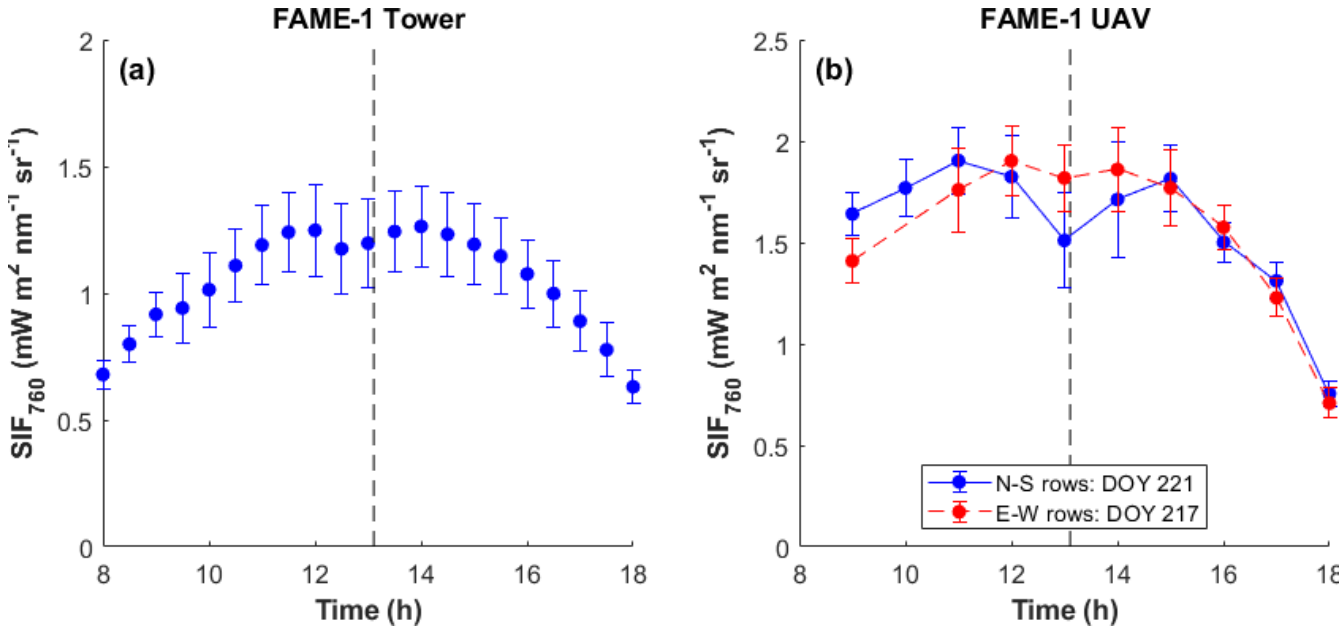

Figure 1. Diurnal dynamics of SIF measured over CMRF. a) SIF_{760} retrieved from the FAME-1 tower during clear days at peak growing season from the FAME-1 tower. b) SIF_{760} retrieved from the FAME-1 UAV flown over two corn fields at CMRF with north-south (N-S) or east-west (E-W) row orientation. Here, SIF is retrieved using SFM_{narrow} (759.5-761.5 nm). For a), markers indicate half-hour average of all clear sky measurements recorded over 2019 from peak growing season (DOY 200 to DOY 250). For b), markers represent average for 6 plots for N-S field or 5 plots for E-W field measured in 2019. Error bars in both panels indicate one standard deviation. Dashed vertical lines indicate average solar noon for this location.

To explore whether the row structure indeed contributed to a midday dip in light absorbed by the canopy, we first contrasted the canopy APAR and fPAR at CMRF and MOFLUX (Fig. 2). Since the SIF tower at MOFLUX is installed over a mature, closed, deciduous forest canopy, we anticipated no midday dip in that data. As observed with SIF (Fig. 1), the measurements of APAR recorded in the N-S row-oriented field at CMRF exhibited a midday dip at approximately 13 h, local solar noon (Fig. 2a), which was due to a midday dip in fPAR (Fig. 2c). In comparison, measurements recorded at MOFLUX did not exhibit a midday dip in APAR (Fig. 2b) or fPAR (Fig. 2d).

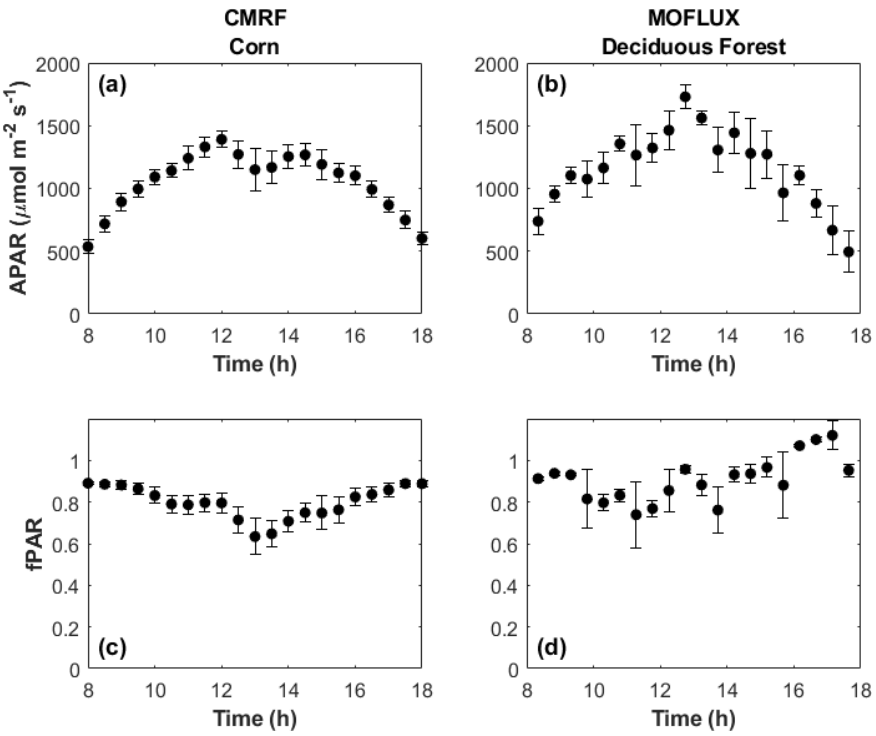

Figure 2. Absorbed photosynthetically active radiation (APAR, top row) and fraction of absorbed photosynthetically active radiation (fPAR, bottom row) at (a,c) CMRF and (b,d) MOFLUX sites on clear-sky conditions. Data shown for panels (a,c) were measured concurrently with 2019 SIF measurements presented in Fig. 1a. The corn field measured by the tower at CMRF has N-S row orientation. Points indicate half-hourly average of instantaneous measurements for CMRF and MOFLUX. Error bars in all panels indicate one standard deviation.

Canopy structure also affects the probability of photons escaping from the canopy (ε), which influences the amount of SIF that can be retrieved from above the canopy. Here we estimated ε as the ratio between NIRv and fPAR according to Eq. 5c (Fig. 3). A midday decrease was observed for both NIR_V (Fig. 3b) and fPAR (Fig. 2c) but produced a net outcome of a midday spike (rather than dip) in ε (Fig. 3a). This was because the diurnal pattern of NIR_V (Fig. 3b), calculated as the product of NDVI and ρ_{NIR} according to Eq. 5b, was dominated by the gradual diurnal pattern of ρ_{NIR} (Fig. 3d). Note that NDVI also exhibited a minor dip at midday, possibly due to the reflectance of bare soil at noon time (Fig. 4c). This midday increase in ε might therefore reflect a systematic bias due to the contamination of NDVI by bare soil at midday when light can actually penetrate to the ground, since light is almost fully intercepted by the canopy at other times of day (Fig. 2c). Alternatively, the increase in ε may act to slightly offset decrease in fPAR when solar position aligns with gaps in the canopy (e.g. row structures), although in our case it could not fully compensate for fPAR and resulted in the midday dip in SIF in the N-S field (Fig. 1). To aid conceptualization of the impacts of row structure and row orientation on light interception by canopy and bare soil, we provide a simplified video illustration of light interception on a summer day across N-S vs. E-W row orientations in Fig. S3. As shown in the video, sunlight hits bare soil at midday in the N-S scenario at both latitudes. In contrast, E-W rows are shaded at midday, indicating that there is no loss of APAR that could result in a midday dip of SIF. Note that sunlight does not hit bare soil at all in the E-W field at the equatorial latitude, while it partially illuminates soil along E-W rows at the higher latitude in the morning

and late afternoon. The difference in patterns of diurnal light interception in the E-W field will vary based on season due to changing solar azimuth angles.

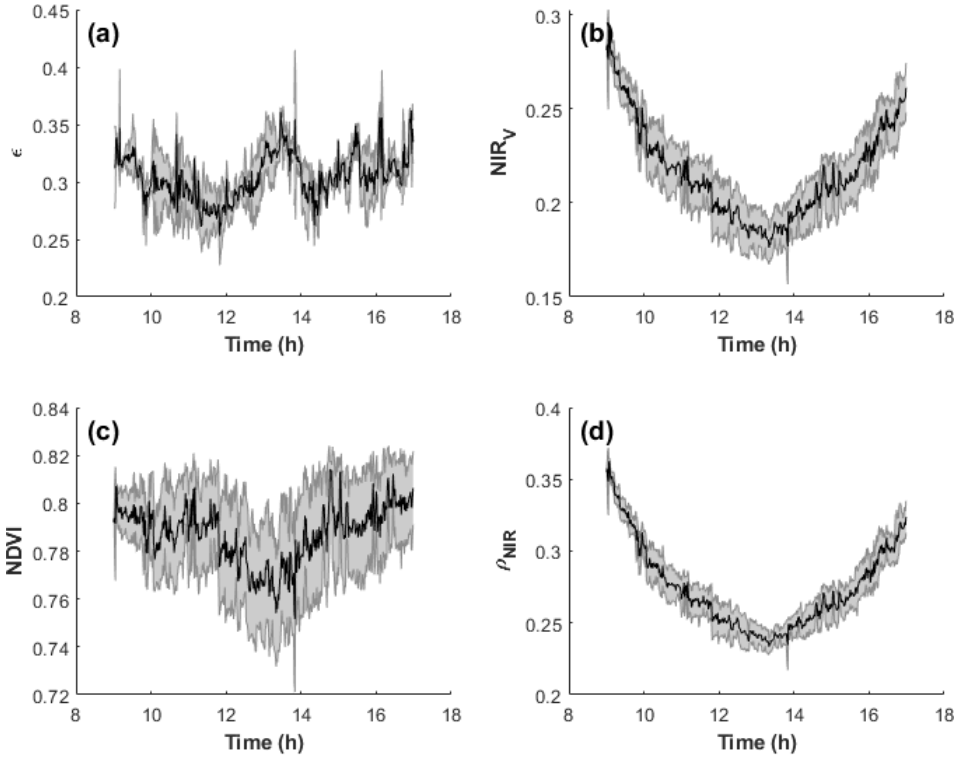

Figure 3. Diurnal patterns of a) canopy escape probability (ε), b) near-infrared radiance of vegetation (NIR_V), c) normalized difference vegetation index (NDVI) and near-infrared reflectance (ρ_{NIR}) recorded by FAME-1 over a N-S oriented corn field at CMRF. Measurements indicate average (black line) and one standard deviation (gray shading) recorded by FAME-1 over five clear days of the peak growing season in 2019.

The diurnal patterns in APAR caused by crop row orientations alter diurnal physiological responses within the canopy. Here we demonstrated this using leaf level measurements of ChlF (Fig. 4). At the top of the canopy, in both N-S and E-W fields, the quantum yields of photosynthesis (Φ_{PSII}) and NPQ (Φ_{NPQ}) followed a "bow-shaped" diurnal pattern, indicating a gradual diurnal induction and relaxation of NPQ in response to the gradual movement of the sun (Fig. 4a,c). However, at the middle canopy position, a striking difference in the energy partitioning was observed between N-S and E-W row-oriented fields, i.e., Φ_{NPQ} spiking precisely

543 at midday due to a larger proportion of leaves (within the canopy) receiving direct light exposure
544 as the sun positioned directly over the row for the former (Fig. 4c) while "bow-shaped" pattern
545 for the latter (Fig. 4d). Φ_F, in general, exhibited a decrease concurrent with Φ_{NPQ} increase for
546 both top- and mid-canopy in both row orientations (Fig. 4, insets). These results suggest that
547 increased NPQ activities can draw energy away from SIF emission of leaves positioned at the
548 top- and mid- canopy.

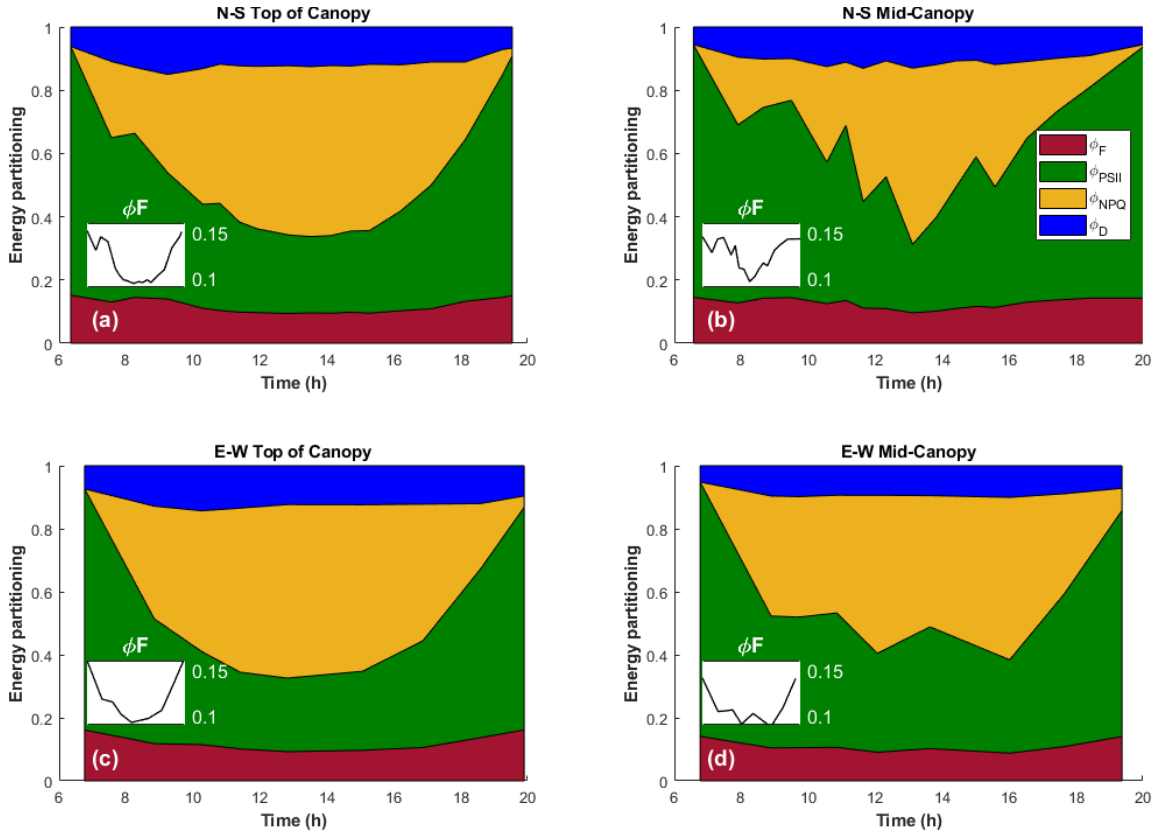

549

550 **Figure 4. Energy partitioning in top of canopy and mid-canopy leaves of corn planted in**
551 **(a,b) N-S or (c,d) E-W row orientation.** Measurements were taken at CMRF on DOY 236 in
552 2018 (for N-S) and DOY 217 in 2019 (E-W). Lines indicate average of 5-6 leaves at the top (a,c)
553 or mid canopy (b,d) position in each field. Panel insets highlight the diurnal patterns of Φ_F.

554 ***3.2 Mechanistically disentangling the impacts of canopy structure and plant physiology on***
555 ***diurnal SIF dynamics***

We used the mechanistic SIF model (Eqs. 2f and 3) to parse the interactive influences of the structural and physiological factors on diurnal SIF dynamics. This was performed using three simulations informed by SIF, hyperspectral reflectance, fPAR, and leaf-level chlorophyll fluorescence measurements acquired at CMRF (Fig. 6, Table 4). Here, canopy structural aspects were represented by APAR and ε, while physiological factor was represented by Φ_F.

The multi-layer simulated NPQ_L, qL_L, and $\Phi_{F,L}$ are shown in Fig. 5. Prominent leaf-level diurnal variations in NPQ, qL, and Φ_F were observed across the vertical canopy. Layers positioned higher in the canopy exhibited lower qL and higher NPQ than lower canopy layers, and a smooth diurnal shape (particularly at the top of the canopy) following the diurnal pattern of incident PAR. This pattern of NPQ is consistent with our leaf-level measurements at the top of the canopy (Fig. 3a). Conversely, layers positioned lower in the canopy exhibited a distinctive peak shape (for NPQ; inverted for qL) at midday due to the influence of canopy structure on APAR, consistent with results from our leaf-level measurements (Fig. 3b and inset). Together, these two interacting physiological processes result in a diurnal midday peak in $\Phi_{F,L}$ for layers in lower canopy, but a midday dip in $\Phi_{F,L}$ for layers at the top of the canopy (Fig. 5c).

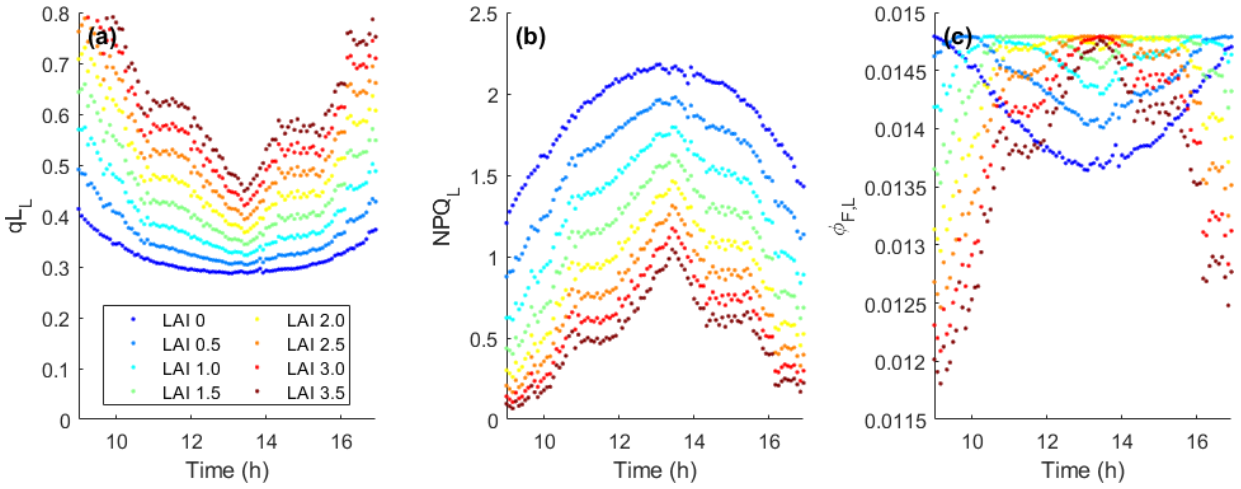

Figure 5. qL, NPQ, and Φ_F generated for eight canopy layers from top (LAI = 0) to bottom of the canopy. Total canopy LAI is assumed to be 4 for simulation purposes. The simulation

approach is described in section 2.4.3. Each layer represents a canopy optical depth of LAI = 0.5, e.g., the legend "LAI = 0" represents the layer from top of the canopy (i.e., LAI = 0) to LAI = 0.5.

Using the full combination of structural and physiological factors, i.e. APAR, ε and Φ_F, the simulated diurnal SIF pattern was highly consistent with measured SIF ($R^2 = 0.80$) (Fig. 6a). When Φ_F did not diurnally vary, there were no detectable changes in performance (Fig. 6b). This indicates that diurnal variations in leaf-level or even sub-canopy layer physiology (NPQ, qL) become greatly attenuated when they are integrated at the canopy level; such effects tend to cancel out (Gu et al., 2019a). Indeed, the opposing diurnal patterns of Φ_F at different canopy layers (Fig. 5c) may help to illustrate why total canopy SIF exhibits such an attenuated midday dip. Furthermore, if only diurnal variation in APAR (and not ε) was accounted for, the performance of the SIF model decreased considerably, although APAR is clearly responsible for the major diurnal variability of SIF ($R^2 = 0.70$, Fig. 6c). The dominance of APAR in the SIF signal has been previously demonstrated, particularly at seasonal scales (Yang et al. 2018, Dechant et al. 2020). In this study, we wish to highlight importance of contributions from the interactive dependence of physiological variations on the sub-canopy light environment shaped by canopy structures and row orientations. Note that even though the presence or absence of diurnal variation of Φ_F did not greatly influence the SIF diurnal dynamics in our simulations, it is still critical to obtain an accurate diurnal mean of Φ_F to obtain the correct magnitude of SIF according to Eq. 3.

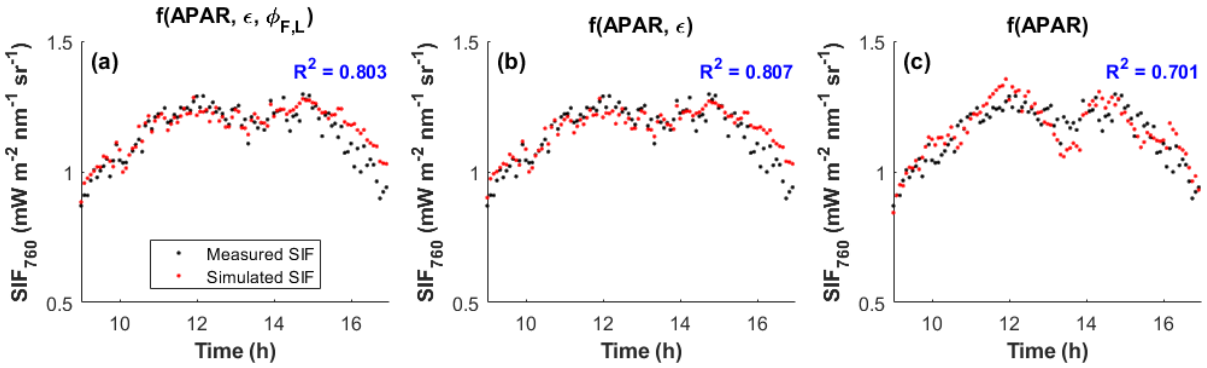

Figure 6. Diurnal pattern of measured SIF_{760} contrasted with SIF_{760} retrieved using SFM_{narrow}, simulated using three combinations of structure and physiology factors. The function shown above each panel indicates which actual measurements were included in the simulation; factors not shown in the function were held constant. R^2 value is shown for correlation between simulated and measured SIF.

3.3 Confounding impacts on measured diurnal SIF dynamics from instrument configuration and retrieval methods

We also attempted to identify impacts on diurnal SIF dynamics caused by the instrument or retrieval method (Fig. 7) that may subsequently confound an accurate attribution to environmental/eco-physiological factors. In a previous work, we identified that atmospheric conditions may influence far-red SIF retrieval using the telluric oxygen absorption band (traditionally ~759-770 nm) (Chang et al., 2020a), and showed that such influence can be mitigated by adjusting the fitting window to a narrower range (e.g. 759.5-761.5 nm). Hence, here we tested SIF retrieved with the spectral fitting method using both wide (SFM_{wide}) and adjusted narrow (SFM_{narrow}) fitting windows. We also contrasted two instrument configurations, the bi-hemispherical FAME, and the hemispherical-conical FloX system, which were each deployed at two distinct sites. We compared an average of 6-11 clear days per year from peak growing season across the four sites (Fig. 7).

From FAME-1, using the traditional fitting window, we observed a midday dip which resulted in an approximately 30% reduction in SIF magnitude at midday (Fig. 7a), which we have observed in a previous study with the same system (Chang et al., 2020a) and appear to be attributed to distortion at the edges of the O_2A well. When using the adjusted fitting window (SFM_{narrow}, as shown in Fig. 1), the severity of the dip was greatly dampened albeit still apparent; also, the overall magnitude of SFM_{narrow} increased, particularly at midday. Interestingly, a milder dip or flattened peak shape was observed in SIF retrieved using FAME-2 using SFM_{wide} (Fig. 7b), but not either of the FloX instruments (Fig. 7c-d). The pattern observed by FAME-2 disappeared when SIF was retrieved using SFM_{narrow}. We also found that the magnitude difference between SFM_{wide} and SFM_{narrow} was greater for the bi-hemispherical system. While in this study we only used SFM to retrieve SIF, we have previously found that other O_2A-based retrieval methods (such as Fraunhofer line discrimination method, FLD, and singular vector decomposition, SVD) are also susceptible to error due to distortion and are therefore likely to exhibit similar performance degradation (Chang et al., 2020a). As we can see in Fig. 7a-b, these distortion effects can potentially mimic or exacerbate natural diurnal patterns such as the midday dip (Fig. 7a). Consequently, their greater impacts could be misattributed to canopy structural or physiological influences, which may still underlie the signal but not actually produce such a dramatic effect. Note that the total magnitude of SIF differs among the four sites due in part to the disparate vegetative targets, climates/environments and growth conditions. The intention of this figure is to compare retrieval method and system impacts on the detected SIF signal, not total magnitude of SIF.

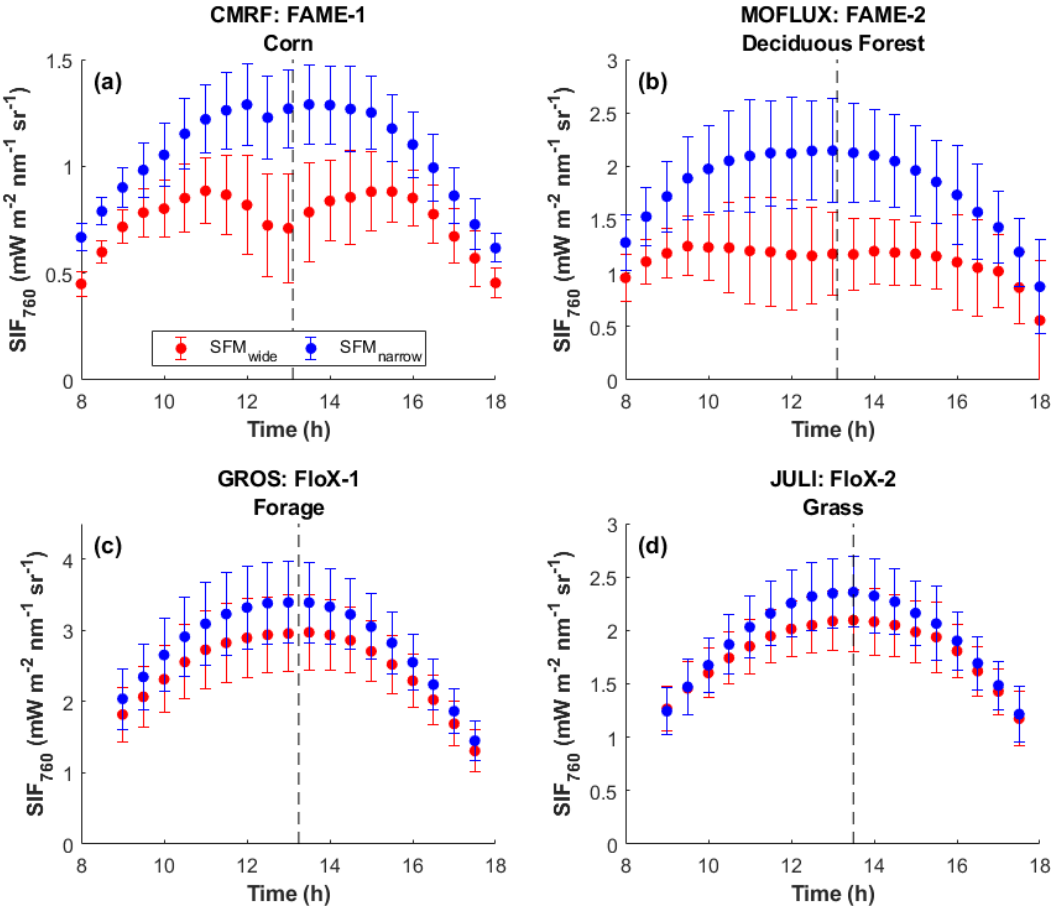

Figure 7. Diurnal SIF dynamics retrieved using traditional and adjusted SFM fitting windows by bi-hemispherical (FAME) and hemispherical-conical (FloX) system configurations. (a) Measurements collected by FAME-1 over a corn field; points indicate average of 3-6 clear days per year recorded over 2018-2019 from peak growing season. (b) Measurements obtained by FAME-2 over a deciduous forest; points indicate average of 11 clear days during May-June of 2017. (c) Measurements obtained by FloX-1 over a site consisting of alfalfa and forage; points indicate average of 8 clear days recorded over April-June of 2018. (d) Measurements obtained by FloX-2 over a grass site; points indicate average of 12 clear days recorded over April-May of 2018. The dashed vertical lines indicate the average time of solar noon across all clear days; error bars indicate standard deviation. Red markers denote SIF retrieved using the wide fitting window (759-767.76 nm); blue markers denote SIF retrieved using the adjusted narrow fitting window (759.5-761.5 nm for FAME, 758-764 nm for FloX). Note that the y-axes have different scaling.

4. Discussion

4.1 Diurnal dynamics of SIF are driven by a combination of canopy structure and physiology

Our comprehensive analysis of the FAME-1 site using tower, UAV, leaf-level measurements and mechanistic modeling enabled us to understand the interactive structural and physiological impacts on diurnal SIF dynamics. Several recent studies have stated that canopy structure, i.e. APAR, drives diurnal SIF dynamics retrieved from ground-based towers (Dechant et al., 2020; Z. Li et al., 2020; Miao et al., 2018; Yang et al., 2018). Here, we have shown that canopy structure not only directly shape the diurnal dynamics of SIF via APAR, but also exert a strong diurnal influence on the within-canopy response of photochemistry and non-photochemistry (Fig. 5a,b) and therefore SIF (Fig. 5,c). However, the impacts of diurnal variations in physiology on SIF are greatly attenuated at the canopy scale (Fig. 6a) due to the opposing responses of Φ_F at different positions within the canopy (Fig. 5c). This finding underscores the complexity of interactions between canopy structure and leaf physiology within the vertical canopy.

Several studies have demonstrated the critical impact of physiology on SIF by forcing a decoupling between photosynthetic CO_2 assimilation and SIF. In a non-stressed, non-light-limited environment, qL decreases while NPQ increases as light intensity increases (Baker, 2008). Chlorophyll fluorescence accommodates the energy remainder caused by the difference between rates of NPQ activation and qL decrease at lower light intensities, but otherwise remains fairly constant (van der Tol et al., 2014). Acebron et al. (2021) utilized *Arabidopsis* NPQ knockout mutants to demonstrate that leaf-level SIF is enhanced while NPQ is inhibited and photochemistry remains constant. In NPQ-intact plants, leaf-level SIF initially increased when photochemistry is rapidly inhibited due to cold shock and the slower NPQ response was not yet induced. Pinto et al. (2020) and Marrs et al. (2020) both artificially inhibited photosynthesis; the former study applied an herbicide which inhibited photosynthetic electron transfer to a grass lawn, while the latter study induced stomatal closure in trees using direct application of abscisic

675 acid and by inducing xylem embolism. In both studies, SIF and NPQ also rapidly increased when
676 photosynthesis decreased. It is evident from these leaf-level studies that the magnitude of Φ_F
677 (and therefore SIF) is highly responsive to the regulation of both photosynthesis and NPQ at the
678 leaf scale. Our multi-layered simulation revealed that at the canopy level in an unstressed corn
679 field, the influences of physiology on diurnal SIF are attenuated because of counteracting
680 responses of qL and NPQ across different layers. However, substantially greater physiological
681 impacts on SIF may well be expected during extreme stress, which warrants future investigation.

682 ***4.2 Agricultural canopy structures influence the diurnal patterns of SIF***

683 Our findings also illustrate the unique influence that the structure of agricultural rows can
684 have upon both leaf-level physiology and canopy-level SIF. Here, we observed how increased
685 light exposure at midday enhanced the induction of NPQ at midday in mid-canopy leaves of a
686 north-south row-oriented corn field. In our unstressed, rainfed corn field, this resulted in lower
687 Φ_{PSII} and Φ_F (Fig. 4); however, as Acebron et al. (2021) demonstrated, under stress conditions
688 when NPQ is unable to fully compensate for excess absorbed light energy when qL decreases,
689 SIF would increase. Previous studies have found that row orientation can affect interception of
690 direct-beam radiation in row crops (Steiner 1987, Hunter et al. 2016, Campos et al. 2016), which
691 in turn influences development, photosynthesis, competitiveness against weeds, and crop yield
692 (Drouet et al. 1999, Liu & Song 2012, Borger et al. 2010, 2016, Hunter et al. 2016). Further
693 studies are needed to characterize the physiological/biological impacts of row structure on
694 biomass, photosynthetic efficiency, water use leading to changes in crop yield.

695 Note that the midday dip of SIF presented here was observed using a bi-hemispherical
696 system over a corn field (Fig. 7a) and was absent when using a similar bi-hemispherical system
697 over a forest (Fig. 7b). Row structures impact the bidirectional reflectance factor (BRF) which

698 changes across viewing and solar zenith angles, as discussed by Zhao et al. (2010, 2016). This
699 influence has been studied using hemispherical-conical systems (Liu et al., 2016; Zhao et al.,
700 2015, 2016). However, diurnal changes in BRF which affect SIF may not be consistent between
701 hemispherical-conical and bi-hemispherical systems. Even if both systems are pointed nadir, the
702 wide field of view of the downward-pointing sensor in bi-hemispherical systems essentially
703 averages across multiple viewing zenith angles of hemispherical-conical systems. It has been
704 shown that hemispherical-conical BRF and SIF vary both diurnally and across viewing zenith
705 angles (Liu et al., 2016). Elucidating the comparative behavior of BRF measured by bi-
706 hemispherical and hemispherical-conical systems will require further investigation using 3d
707 radiative transfer models and would benefit from an *in situ* side-by-side system comparison.

708 Furthermore, the productivity of east-west and north-south row orientations can vary based
709 on latitude and season. For example, optimization of row orientation has been shown to provide
710 up to 25% higher yield in corn, but the optimal orientation differs from high to low latitudes
711 (Borger et al. 2016, Borger et al. 2010, Mutsaers 1980). To illustrate this effect, we generated a
712 video demonstrating the movement of light and shadows of the sun across N-S and E-W row
713 structures at a higher latitude and an equatorial latitude on a day in mid-July (Fig. S3). From this
714 illustration, it is clear that row structure and orientation can greatly impact the consistency of
715 light interception across the day. Note that the impact of row structure on light interception is
716 dependent upon the height of the crop, row spacing and canopy closure. For corn, even at full
717 canopy closure, the canopy is not dense enough to fully intercept all light when the sun is
718 positioned directly overhead, leading to the midday dip in APAR that we observed.
719 Consequently, we suggest that crop row orientation, a highly important agricultural management
720 strategy in the agronomy community, may exert a yet-unexplored influence on satellite SIF

721 retrieved over agricultural fields that would affect certain crops/regions more than others. It is
722 also expected that these row structure effects will change across the growing season, as a larger
723 proportion of light will penetrate through younger crops prior to canopy closure, and therefore a
724 stronger row orientation effect may be expected during early growing season. Depending on row
725 spacing, crops may close canopies later in the season, reducing the effect of rows on APAR and
726 SIF.

727 The row structural impacts on SIF may add an additional layer of complexity to interpret SIF
728 retrievals from satellite platforms, because none of the existing satellites with SIF capability are
729 geostationary. Thus, retrieval of SIF from such datasets necessitates the calculation of daily
730 integrals of SIF from their single overpass times. To date, two strategies have been used: 1)
731 assuming the SIF measurement was performed under clear skies and extrapolating the clear-sky
732 patterns using the cosine of the solar zenith angle (such as in Frankenberg et al., 2011; Sun et al.,
733 2018); or 2) calculating the ratio of instantaneous to daily PAR (such as proposed by Hu et al.,
734 2018). However, neither of these approaches can mitigate the impact of row structure on SIF
735 emission, because they only account for PAR and not fPAR, and do not account for
736 physiological changes in NPQ and qL. Fig. 8 illustrates the potential for over- or under-
737 estimation error, depending on specific overpass time, from omitting the diurnal complexity in
738 SIF based on these simple extrapolation approaches for a strongly structured canopy. In this
739 example, utilizing a morning overpass of 9:00 h results in overestimation of daily SIF by 10%,
740 while a midday overpass of 12:00 h underestimates by 27% and the afternoon overpass of 13:30h
741 only underestimates by 4% due to the opposing effects of underestimating in morning and
742 evening while overestimating at midday. These values are presented purely for illustrative
743 purposes but demonstrate how the complexity of diurnal SIF dynamics can greatly impact the

daily integral estimation of satellite SIF. This is currently an insurmountable challenge, since no diurnal fPAR is yet available from satellite platforms. However, the upcoming geostationary platforms with SIF-observing capabilities, e.g., Tropospheric Emissions: Monitoring Pollution (TEMPO) and Geostationary Carbon Observatory (GEOCarb), have strong potential to capture the sub-daily variations in SIF as well as fPAR, and can therefore provide insights on how to scale the existing SIF retrievals from sun-synchronized platforms to daily integrals in a more physiologically realistic way.

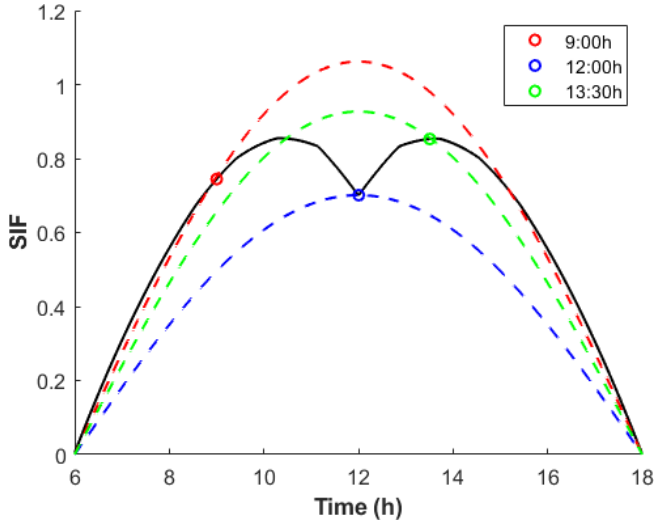

Figure 8. Illustration of potential for over- or under-estimation of SIF using a daily integral of the cosine of the solar zenith angle. Colored points represent different satellite overpass times (9:00, 12:00, 13:30 h). Colored dashed lines indicate SIF extrapolated from each point using the cosine of the solar zenith angle. The black line is a representation of a "true" SIF signal in a N-S oriented agricultural field, such as observed in our study.

4.3 Instrument configuration and retrieval method influence retrieval of diurnal SIF

Our findings demonstrate that two non-biological factors, the instrument configuration used and the retrieval method, can heavily influence the diurnal shape and magnitude of retrieved SIF. Previous studies (Liu & Liu, 2017; Sabater et al., 2018) have identified a distortion effect caused by atmospheric in-filling that specifically affects SIF retrieved from telluric oxygen bands. In this study, we observed that bi-hemispherical configurations tend to exhibit greater susceptibility

763 to such in-filling effects, with clear underestimation of SIF even close to the canopy (1.5-2 m)
764 when retrieved using the spectral fitting method and traditional wide fitting window covering the
765 entire O_2A band. We were able to mitigate this effect following the protocol developed in our
766 previous study (Chang et al., 2020a) by reducing the width of the fitting window (Fig. 7).

767 Interestingly, the difference in magnitude of SIF retrieved using SFM_{wide} and SFM_{narrow} from
768 the FAME-2 site deployed 32 m above the target forest canopy (Fig. 7d), was no greater than the
769 difference in SIF retrieved using the two methods at FAME-1. This result, together with the
770 much smaller difference between SFM_{wide} and SFM_{narrow} reported from both FloX sites, suggests
771 that the source of the distortion in this study is likely from impacts of diffuse radiation on the
772 shoulders of the telluric oxygen bands, rather than the depth of the atmospheric column itself.
773 Naturally, bi-hemispherical systems such as the FAME will collect more diffuse radiation from
774 the much wider field of view using a cosine corrector, and therefore would be more susceptible
775 to such distortion effects. This result concurs with our previous study, where we compared
776 FAME-1 with a different hemispherical-conical system (PhotoSpec, Grossmann et al. 2018) and
777 observed a greater impact of diffuse radiation from variable atmospheric conditions on the
778 retrieval of SIF from FAME-1. Another study by Zhang et al. (2019) compared several bi-
779 hemispherical and hemispherical-conical systems. While their study did not discuss the impacts
780 of diffuse radiation on SIF retrieval, they also presented some evidence that bi-hemispherical
781 systems exhibit greater distortion around the edges of the oxygen bands than hemispherical-
782 conical configured systems.

783 It is important to point out that whether the bi-hemispherical or hemispherical-conical
784 systems should be used depend on the research objectives. The bi-hemispherical system, whose
785 SIF signal is from a large footprint, should be the option when the objective is to complement

786 eddy flux observations for ecosystem process studies (Gu et al. 2019b). In contrast, the
787 hemispherical-conical system, which has a much smaller footprint, may offer better matching
788 potential if the objective is to validate the satellite measurements. Theoretically, the differences
789 in the measured SIF between the bi-hemispherical and hemispherical-conical systems can be
790 reconciled through advances in retrieval methods and SIF radiative transfer modeling. Such
791 advances are much needed.

792 ***4.4 Limitations and future directions***

793 One limitation of this study is that its scope was constrained by limited data availability from
794 the MOFLUX, GROS and JULI sites. We did not obtain diurnal leaf level measurements at these
795 three sites. Furthermore, the lack of APAR measurements from GROS and JULI precluded our
796 ability to calculate ε for these two sites, while the lack of hyperspectral measurements from
797 MOFLUX precluded our ability to calculate NIR_V for this site. Thus, we were unable to perform
798 SIF simulations for these three datasets, although it would be certainly of great interest to
799 evaluate whether the model and findings hold across sites and instruments. This may be
800 examined in future work with growing availability of additional measurements.

801 Another limitation of the study is contained within the empirical formulation of the NPQ and
802 qL models used in the estimation of the physiological component in the SIF model. Here we use
803 parsimonious light response models for both NPQ and qL; however, both variables in reality
804 respond to a variety of environmental factors including light intensity, temperature, water,
805 nutrient availability, and CO_2 (Cendrero-Mateo et al., 2015; Chang et al., 2016; Porcar-Castell,
806 2011; Takahashi et al., 2021; Yamori et al., 2011). A realistic model formulation would include
807 these factors as well. For the purposes of this study (illustrating the contribution of the
808 physiological component to diurnal SIF), we considered the light response function sufficiently

809 capture the first order pattern, as there were no heat, drought, or nutrient stress during our
810 measurement periods.

811 We have shown in this study that mechanistic modeling of the dynamics of SIF at the canopy
812 scale requires understanding not only of photosynthesis and NPQ at the leaf level but also an
813 understanding of behavior of leaves across positions within the vertical canopy, which may be
814 exposed to different light and even leaf temperature depending on sunlit or shaded status. These
815 varying microenvironments will influence both photosynthesis and NPQ and consequently SIF
816 dynamics. Future studies exploring the effects of stress within the vertical canopy across
817 different plant species are warranted to support efforts to scale from leaf to canopy.

818 **5. Conclusions**

819 In this study, we have mechanistically attributed the dynamics of diurnal SIF to canopy light
820 absorption, canopy escape probability, plant physiology, and additional confounding factors
821 from instrumental configuration and retrieval methods. We have shown that canopy architecture
822 and agricultural row structures, which govern diurnal APAR, can introduce a distinctive diurnal
823 midday dip, even in the absence of stress. These diurnal patterns in APAR strongly influence
824 within-canopy variations in photochemistry, nonphotochemical quenching and fluorescence
825 emission. However, these variations at the leaf level or from sub-canopy layers are attenuated
826 once they become integrated at the canopy scale. Furthermore, we have demonstrated that SIF
827 instrument configuration and retrieval method can cause underestimation and exaggeration of
828 diurnal features in measured diurnal SIF. Thus, care must be taken for physiologically
829 meaningful interpretation of diurnal SIF dynamics. Our study highlights the necessity to account
830 for these factors to accurately upscale satellite SIF from instantaneous to daily integrals, and

831 informs future synthesis work with different SIF instrumentation and retrieval methods across
832 sites.

833 **Acknowledgments**

834 This work was supported by USDA-NIFA grant (2018-67012-27985), NSF Macrosystem
835 Biology (Award 1926488), USDA-NIFA Hatch Fund (1014740), and the Cornell Initiative for
836 Digital Agriculture Research Innovation Fund. C. Chang acknowledges support from the U.S.
837 Department of Agriculture, Agricultural Research Service. L. Gu and J.D. Wood acknowledge
838 support from the U.S. Department of Energy, Office of Science, Office of Biological and
839 Environmental Research Program, Climate and Environmental Sciences Division through Oak
840 Ridge National Laboratory's Terrestrial Ecosystem Science (TES) Science Focus Area (SFA).
841 Field measurements with FloX units were carried out under lead management and funding of
842 ESA in the frame of AtmoFLEX (4000122454/17/NL/FF/mg). The authors gratefully
843 acknowledge the expertise and support of Paul Stachowski and Jeff Stayton at CMRF for farm
844 management, and the support of Andreas Burkart, Tommaso Julitta, and Uwe Rascher for
845 installations of FloX at GROS and JULI. Following paper acceptance, data from CMRF will be
846 made publicly available on the Cornell eCommons data repository; meteorological data from
847 MOFLUX are publicly available from Ameriflux, and SIF data from MOFLUX will be made
848 available on Cornell eCommons; data from GROS and JULI will be made available by the
849 European Space Agency (ESA), repository to be determined.

850

851 **References**

852 Acebron, K., Matsubara, S., Jedmowski, C., Emin, D., Muller, O., & Rascher, U. (2021). Diurnal

dynamics of nonphotochemical quenching in Arabidopsis npq mutants assessed by solar-induced fluorescence and reflectance measurements in the field. *New Phytologist*, *229*(4), 2104–2119. https://doi.org/10.1111/nph.16984

Anav, A., Friedlingstein, P., Beer, C., Ciais, P., Harper, A., Jones, C., Murray-Tortarolo, G., Papale, D., Parazoo, N. C., Peylin, P., Piao, S., Sitch, S., Viovy, N., Wiltshire, A., & Zhao, M. (2015). Reviews of Geophysics primary production : A review. *Reviews of Geophysics*, 1–34. https://doi.org/10.1002/2015RG000483.Received

Atherton, J., Nichol, C. J., & Porcar-Castell, A. (2016). Using spectral chlorophyll fluorescence and the photochemical reflectance index to predict physiological dynamics. *Remote Sensing of Environment*, *176*(1), 17–30. https://doi.org/10.1016/j.rse.2015.12.036

Awal, M. A., Koshi, H., & Ikeda, T. (2006). Radiation interception and use by maize/peanut intercrop canopy. *Agricultural and Forest Meteorology*, *139*(1–2), 74–83. https://doi.org/10.1016/j.agrformet.2006.06.001

Baker, N. R. (2008). Chlorophyll fluorescence: a probe of photosynthesis in vivo. *Annual Review of Plant Biology*, *59*, 89–113. https://doi.org/10.1146/annurev.arplant.59.032607.092759

Beer, C., Reichstein, M., Tomelleri, E., Ciais, P., Jung, M., Carvalhais, N., Rödenbeck, C., Arain, M. A., Baldocchi, D., Bonan, G. B., Bondeau, A., Cescatti, A., Lasslop, G., Lindroth, A., Lomas, M., Luyssaert, S., Margolis, H., Oleson, K. W., Roupsard, O., … Papale, D. (2010). Terrestrial gross carbon dioxide uptake: Global distribution and covariation with climate. *Science*. https://doi.org/10.1126/science.1184984

Bendig, J., Malenovsky, Z., Gautam, D., & Lucieer, A. (2019). Solar-Induced Chlorophyll Fluorescence Measured From an Unmanned Aircraft System: Sensor Etaloning and

875 Platform Motion Correction. *IEEE Transactions on Geoscience and Remote Sensing*, 1–8.
876 https://doi.org/10.1109/TGRS.2019.2956194

877 Björkman, O., & Demmig, B. (1987). Photon yield of O2 evolution and chlorophyll fluorescence
878 characteristics at 77 K among vascular plants of diverse origins. *Planta*, *170*(4), 489–504.
879 https://doi.org/10.1007/BF00402983

880 Burkart, A., Schickling, A., Mateo, M. P. C., Wrobel, T. J., Rossini, M., Cogliati, S., Julitta, T.,
881 & Rascher, U. (2015). A Method for Uncertainty Assessment of Passive Sun-Induced
882 Chlorophyll Fluorescence Retrieval Using an Infrared Reference Light. *IEEE Sensors*
883 *Journal*, *15*(8), 4603–4611. https://doi.org/10.1109/JSEN.2015.2422894

884 Campbell, P. K. E., Huemmrich, K. F., Middleton, E. M., Ward, L. A., Julitta, T., Daughtry, C.
885 S. T., Burkart, A., Russ, A. L., & Kustas, W. P. (2019). Diurnal and Seasonal Variations in
886 Chlorophyll Fluorescence Associated with Photosynthesis at Leaf and Canopy Scales.
887 *Remote Sensing*, *11*(5), 488. https://doi.org/10.3390/rs11050488

888 Cendrero-Mateo, M. P., Carmo-Silva, A. E., Porcar-Castell, A., Hamerlynck, E. P., Papuga, S.
889 A., & Moran, M. S. (2015). Dynamic response of plant chlorophyll fluorescence to light,
890 water and nutrient availability. *Functional Plant Biology*, *42*(8), 746–757.
891 https://doi.org/10.1071/FP15002

892 Cendrero-Mateo, M. P., Wieneke, S., Damm, A., Alonso, L., Pinto, F., Moreno, J., Guanter, L.,
893 Celesti, M., Rossini, M., Sabater, N., Cogliati, S., Julitta, T., Rascher, U., Goulas, Y.,
894 Aasen, H., Pacheco-Labrador, J., & MacArthur, A. (2019). Sun-Induced Chlorophyll
895 Fluorescence III: Benchmarking Retrieval Methods and Sensor Characteristics for Proximal
896 Sensing. *Remote Sensing*, *11*(8), 962. https://doi.org/10.3390/rs11080962

Chang, C. Y.-Y., Fréchette, E., Unda, F., Mansfield, S. D., & Ensminger, I. (2016). Elevated temperature and CO2 stimulate late season photosynthesis but impair cold hardening in pine. *Plant Physiology*, *172*(2), pp.00753.2016. https://doi.org/10.1104/pp.16.00753

Chang, C. Y.-Y., Guanter, L., Frankenberg, C., Köhler, P., Gu, L., Magney, T. S., Grossmann, K., & Sun, Y. (2020). Systematic assessment of retrieval methods for canopy far-red solar-induced chlorophyll fluorescence (SIF) using high-frequency automated field spectroscopy. *Journal of Geophysical Research: Biogeosciences*. https://doi.org/10.1029/2019JG005533

Chang, C. Y.-Y., Zhou, R., Kira, O., Marri, S., Skovira, J., Gu, L., & Sun, Y. (2020). An Unmanned Aerial System (UAS) for concurrent measurements of solar-induced chlorophyll fluorescence and hyperspectral reflectance toward improving crop monitoring. *Agricultural and Forest Meteorology*, *294*, 108145. https://doi.org/10.1016/j.agrformet.2020.108145

Cogliati, S., Celesti, M., Cesana, I., Miglietta, F., Genesio, L., Julitta, T., Schuettemeyer, D., Drusch, M., Rascher, U., Jurado, P., & Colombo, R. (2019). A Spectral Fitting Algorithm to Retrieve the Fluorescence Spectrum from Canopy Radiance. *Remote Sensing*, *11*(16), 1840. https://doi.org/10.3390/rs11161840

Cogliati, S., Rossini, M., Julitta, T., Meroni, M., Schickling, A., Burkart, A., Pinto, F., Rascher, U., & Colombo, R. (2015). Continuous and long-term measurements of reflectance and sun-induced chlorophyll fluorescence by using novel automated field spectroscopy systems. *Remote Sensing of Environment*, *164*, 270–281. https://doi.org/10.1016/j.rse.2015.03.027

Colombo, R., Celesti, M., Bianchi, R., Campbell, P. K. E., Cogliati, S., Cook, B. D., Corp, L. A., Damm, A., Domec, J. C., Guanter, L., Julitta, T., Middleton, E. M., Noormets, A., Panigada, C., Pinto, F., Rascher, U., Rossini, M., & Schickling, A. (2018). Variability of

sun-induced chlorophyll fluorescence according to stand age-related processes in a managed loblolly pine forest. *Global Change Biology*, *24*(7), 2980–2996. https://doi.org/10.1111/gcb.14097

Damm, A., Elber, J., Erler, A., Gioli, B., Hamdi, K., Hutjes, R., Kosvancova, M., Meroni, M., Miglietta, F., Moersch, A., Moreno, J., Schickling, A., Sonnenschein, R., Udelhoven, T., van der Linden, S., Hostert, P., & Rascher, U. (2010). Remote sensing of sun-induced fluorescence to improve modeling of diurnal courses of gross primary production (GPP). *Global Change Biology*, *16*(1), 171–186. https://doi.org/10.1111/j.1365-2486.2009.01908.x

Dechant, B., Ryu, Y., Badgley, G., Zeng, Y., Berry, J. A., Zhang, Y., Goulas, Y., Li, Z., Zhang, Q., Kang, M., Li, J., & Moya, I. (2020). Canopy structure explains the relationship between photosynthesis and sun-induced chlorophyll fluorescence in crops. *Remote Sensing of Environment*, *241*(February). https://doi.org/10.1016/j.rse.2020.111733

Frankenberg, C., Fisher, J. B., Worden, J., Badgley, G., Saatchi, S. S., Lee, J.-E., Toon, G. C., Butz, A., Jung, M., Kuze, A., & Yokota, T. (2011). New global observations of the terrestrial carbon cycle from GOSAT: Patterns of plant fluorescence with gross primary productivity. *Geophysical Research Letters*, *38*(17), L17706. https://doi.org/10.1029/2011GL048738

Frankenberg, C., Köhler, P., Magney, T. S., Geier, S., Lawson, P., Schwochert, M., McDuffie, J., Drewry, D. T., Pavlick, R., & Kuhnert, A. (2018). The Chlorophyll Fluorescence Imaging Spectrometer (CFIS), mapping far red fluorescence from aircraft. *Remote Sensing of Environment*, *217*(September), 523–536. https://doi.org/10.1016/j.rse.2018.08.032

Genty, B., Briantais, J.-M. M., & Baker, N. R. (1989). The relationship between the quantum

yield of photosynthetic electron transport and quenching of chlorophyll fluorescence. *Biochimica et Biophysica Acta - General Subjects*, *990*(1), 87–92. https://doi.org/10.1016/S0304-4165(89)80016-9

Gitelson, A. A., & Gamon, J. A. (2015). The need for a common basis for defining light-use efficiency: Implications for productivity estimation. *Remote Sensing of Environment*. https://doi.org/10.1016/j.rse.2014.09.017

Grossmann, K., Frankenberg, C., Magney, T. S., Hurlock, S. C., Seibt, U., & Stutz, J. (2018). PhotoSpec: A new instrument to measure spatially distributed red and far-red Solar-Induced Chlorophyll Fluorescence. *Remote Sensing of Environment*, *216*(July), 311–327. https://doi.org/10.1016/j.rse.2018.07.002

Gu, L., Han, J., Wood, J. D., Chang, C. Y.-Y., & Sun, Y. (2019). Sun-induced Chl fluorescence and its importance for biophysical modeling of photosynthesis based on light reactions. *New Phytologist*, *223*(3), 1179–1191. https://doi.org/10.1111/nph.15796

Gu, L., Pallardy, S. G., Yang, B., Hosman, K. P., Mao, J., Ricciuto, D., Shi, X., & Sun, Y. (2016). Testing a land model in ecosystem functional space via a comparison of observed and modeled ecosystem flux responses to precipitation regimes and associated stresses in a Central U.S. forest. *Journal of Geophysical Research: Biogeosciences*, *121*(7), 1884–1902. https://doi.org/10.1002/2015JG003302

Gu, L., Wood, J. D., Chang, C. Y.-Y. Y. Y., Sun, Y., & Riggs, J. S. (2019). Advancing Terrestrial Ecosystem Science With a Novel Automated Measurement System for Sun-Induced Chlorophyll Fluorescence for Integration With Eddy Covariance Flux Networks. *Journal of Geophysical Research: Biogeosciences*, *124*(1), 127–146.

https://doi.org/10.1029/2018JG004742

He, L., Magney, T., Dutta, D., Yin, Y., Köhler, P., Grossmann, K., Stutz, J., Dold, C., Hatfield, J., Guan, K., Peng, B., & Frankenberg, C. (2020). From the Ground to Space: Using Solar-Induced Chlorophyll Fluorescence to Estimate Crop Productivity. *Geophysical Research Letters*, *47*(7), 1–12. https://doi.org/10.1029/2020GL087474

Hendrickson, L., Furbank, R. T., & Chow, W. S. (2004). A simple alternative approach to assessing the fate of absorbed light energy using chlorophyll fluorescence. *Photosynthesis Research*, 73–81. https://doi.org/10.1023/B:PRES.0000040446.87305.f4

Hu, J., Liu, L., Guo, J., Du, S., & Liu, X. (2018). Upscaling solar-induced chlorophyll fluorescence from an instantaneous to daily scale gives an improved estimation of the gross primary productivity. *Remote Sensing*, *10*(10). https://doi.org/10.3390/rs10101663

Joiner, J., Yoshida, Y., Vasilkov, A. P., Yoshida, Y., Corp, L. A., & Middleton, E. M. (2011). First observations of global and seasonal terrestrial chlorophyll fluorescence from space. *Biogeosciences*, *8*(3), 637–651. https://doi.org/10.5194/bg-8-637-2011

Julitta, T., Corp, L. A., Rossini, M., Burkart, A., Cogliati, S., Davies, N., Hom, M., Arthur, A. Mac, Middleton, E. M., Rascher, U., Schickling, A., & Colombo, R. (2016). Comparison of sun-induced chlorophyll fluorescence estimates obtained from four portable field spectroradiometers. *Remote Sensing*, *8*(2), 1–14. https://doi.org/10.3390/rs8020122

Köhler, P., Behrenfeld, M. J., Landgraf, J., Joiner, J., Magney, T. S., & Frankenberg, C. (2020). Global Retrievals of Solar-Induced Chlorophyll Fluorescence at Red Wavelengths With TROPOMI. *Geophysical Research Letters*, *47*(15), 1–10. https://doi.org/10.1029/2020GL087541

985 Kramer, D. M., Johnson, G., Kiirats, O., & Edwards, G. E. (2004). New fluorescence parameters
986 for the determination of QA redox state and excitation energy fluxes. *Photosynthesis*
987 *Research*, *79*(2), 209–218. https://doi.org/10.1023/B:PRES.0000015391.99477.0d

988 Li, J., Zhang, Y., Gu, L., Li, Z., Li, J., Zhang, Q., Zhang, Z., & Song, L. (2020). Seasonal
989 variations in the relationship between sun-induced chlorophyll fluorescence and
990 photosynthetic capacity from the leaf to canopy level in a rice crop. *Journal of*
991 *Experimental Botany*, *71*(22), 7179–7197. https://doi.org/10.1093/jxb/eraa408

992 Li, Z., Zhang, Q., Li, J., Yang, X., Wu, Y., Zhang, Z., Wang, S., Wang, H., & Zhang, Y. (2020).
993 Solar-induced chlorophyll fluorescence and its link to canopy photosynthesis in maize from
994 continuous ground measurements. *Remote Sensing of Environment*, *236*(November 2019),
995 111420. https://doi.org/10.1016/j.rse.2019.111420

996 Liu, L., Guan, L., & Liu, X. (2017). Directly estimating diurnal changes in GPP for C3 and C4
997 crops using far-red sun-induced chlorophyll fluorescence. *Agricultural and Forest*
998 *Meteorology*, *232*, 1–9. https://doi.org/10.1016/j.agrformet.2016.06.014

999 Liu, L., Liu, X., Wang, Z., & Zhang, B. (2016). Measurement and Analysis of Bidirectional SIF
1000 Emissions in Wheat Canopies. *IEEE Transactions on Geoscience and Remote Sensing*,
1001 *54*(5), 2640–2651. https://doi.org/10.1109/TGRS.2015.2504089

1002 Liu, X., & Liu, L. (2017). Influence of the canopy BRDF characteristics and illumination
1003 conditions on the retrieval of solar-induced chlorophyll fluorescence. *International Journal*
1004 *of Remote Sensing*, *39*(6), 1782–1799. https://doi.org/10.1080/01431161.2017.1404165

1005 Maddonni, G. A., Otegui, M. E., & Cirilo, A. G. (2001). Plant population density, row spacing
1006 and hybrid effects on maize canopy architecture and light attenuation. *Field Crops*

Research, *71*(3), 183–193. https://doi.org/10.1016/S0378-4290(01)00158-7

Magney, T. S., Barnes, M. L., & Yang, X. (2020). On the Covariation of Chlorophyll Fluorescence and Photosynthesis Across Scales. *Geophysical Research Letters*, *47*(23), 1–7. https://doi.org/10.1029/2020GL091098

Magney, T. S., Bowling, D. R., Logan, B. A., Grossmann, K., Stutz, J., Blanken, P. D., Burns, S. P., Cheng, R., Garcia, M. A., Köhler, P., Lopez, S., Parazoo, N. C., Raczka, B., Schimel, D., & Frankenberg, C. (2019). Mechanistic evidence for tracking the seasonality of photosynthesis with solar-induced fluorescence. *Proceedings of the National Academy of Sciences of the United States of America*, *116*(24), 11640–11645. https://doi.org/10.1073/pnas.1900278116

Marrs, J. K., Reblin, J. S., Logan, B. A., Allen, D. W., Reinmann, A. B., Bombard, D. M., Tabachnik, D., & Hutyra, L. R. (2020). Solar-Induced Fluorescence Does Not Track Photosynthetic Carbon Assimilation Following Induced Stomatal Closure. *Geophysical Research Letters*, *47*(15), 1–11. https://doi.org/10.1029/2020GL087956

Miao, G., Guan, K., Suyker, A. E., Yang, X., Arkebauer, T. J., Walter-Shea, E. A., Kimm, H., Hmimina, G. Y., Gamon, J. A., Franz, T. E., Frankenberg, C., Berry, J. A., & Wu, G. (2020). Varying Contributions of Drivers to the Relationship Between Canopy Photosynthesis and Far-Red Sun-Induced Fluorescence for Two Maize Sites at Different Temporal Scales. *Journal of Geophysical Research: Biogeosciences*, *125*(2), 1–17. https://doi.org/10.1029/2019JG005051

Miao, G., Guan, K., Yang, X., Bernacchi, C. J., Berry, J. A., DeLucia, E. H., Wu, J., Moore, C. E., Meacham, K., Cai, Y., Peng, B., Kimm, H., & Masters, M. D. (2018). Sun-Induced

1029 Chlorophyll Fluorescence, Photosynthesis, and Light Use Efficiency of a Soybean Field
1030 from Seasonally Continuous Measurements. *Journal of Geophysical Research:*
1031 *Biogeosciences*, *123*(2), 610–623. https://doi.org/10.1002/2017JG004180

1032 Niinemets, Ü. (2010). Responses of forest trees to single and multiple environmental stresses
1033 from seedlings to mature plants: Past stress history, stress interactions, tolerance and
1034 acclimation. *Forest Ecology and Management*, *260*(10), 1623–1639.
1035 https://doi.org/10.1016/j.foreco.2010.07.054

1036 Palmer, J. W. (1989). The effects of row orientation, tree height, time of year and latitude on
1037 light interception and distribution in model apple hedgerow canopies. *Journal of*
1038 *Horticultural Science*, *64*(2), 137–145. https://doi.org/10.1080/14620316.1989.11515937

1039 Parazoo, N. C., Frankenberg, C., Köhler, P., Joiner, J., Yoshida, Y., Magney, T., Sun, Y., &
1040 Yadav, V. (2019). Towards a Harmonized Long-Term Spaceborne Record of Far-Red
1041 Solar-Induced Fluorescence. *Journal of Geophysical Research: Biogeosciences*, *124*(8),
1042 2518–2539. https://doi.org/10.1029/2019JG005289

1043 Pinto, F., Celesti, M., Acebron, K., Alberti, G., Cogliati, S., Colombo, R., Juszczak, R.,
1044 Matsubara, S., Miglietta, F., Palombo, A., Panigada, C., Pignatti, S., Rossini, M., Sakowska,
1045 K., Schickling, A., Schüttemeyer, D., Stróżecki, M., Tudoroiu, M., & Rascher, U. (2020).
1046 Dynamics of sun-induced chlorophyll fluorescence and reflectance to detect stress-induced
1047 variations in canopy photosynthesis. *Plant, Cell & Environment*, *43*(7), 1637–1654.
1048 https://doi.org/10.1111/pce.13754

1049 Porcar-Castell, A. (2011). A high-resolution portrait of the annual dynamics of photochemical
1050 and non-photochemical quenching in needles of Pinus sylvestris. *Physiologia Plantarum*,

143(2), 139–153. https://doi.org/10.1111/j.1399-3054.2011.01488.x

Porcar-Castell, A., Tyystjärvi, E., Atherton, J., Van Der Tol, C., Flexas, J., Pfündel, E. E., Moreno, J., Frankenberg, C., & Berry, J. A. (2014). Linking chlorophyll a fluorescence to photosynthesis for remote sensing applications: Mechanisms and challenges. *Journal of Experimental Botany*, *65*(15), 4065–4095. https://doi.org/10.1093/jxb/eru191

Rascher, U., Alonso, L., Burkart, A., Cilia, C., Cogliati, S., Colombo, R., Damm, A., Drusch, M., Guanter, L., Hanus, J., Hyvärinen, T., Julitta, T., Jussila, J., Kataja, K., Kokkalis, P., Kraft, S., Kraska, T., Matveeva, M., Moreno, J., … Zemek, F. (2015). Sun-induced fluorescence - a new probe of photosynthesis: First maps from the imaging spectrometer HyPlant. *Global Change Biology*, *21*(12), 4673–4684. https://doi.org/10.1111/gcb.13017

Sabater, N., Vicent, J., Alonso, L., Verrelst, J., Middleton, E., Porcar-Castell, A., & Moreno, J. (2018). Compensation of Oxygen Transmittance Effects for Proximal Sensing Retrieval of Canopy–Leaving Sun–Induced Chlorophyll Fluorescence. *Remote Sensing*, *10*(10), 1551. https://doi.org/10.3390/rs10101551

Serôdio, J., & Lavaud, J. (2011). A model for describing the light response of the nonphotochemical quenching of chlorophyll fluorescence. *Photosynthesis Research*, *108*(1), 61–76. https://doi.org/10.1007/s11120-011-9654-0

Siegmann, B., Alonso, L., Celesti, M., Cogliati, S., Colombo, R., Damm, A., Douglas, S., Guanter, L., Hanuš, J., Kataja, K., Kraska, T., Matveeva, M., Moreno, J., Muller, O., Pikl, M., Pinto, F., Vargas, J. Q., Rademske, P., Rodriguez-Morene, F., … Rascher, U. (2019). The high-performance airborne imaging spectrometer HyPlant-from raw images to top-of-canopy reflectance and fluorescence products: Introduction of an automatized processing

chain. *Remote Sensing*, *11*(23). https://doi.org/10.3390/rs11232760

Stewart, D. W., Costa, C., Dwyer, L. M., Smith, D. L., Hamilton, R. I., & Ma, B. L. (2003). Canopy Structure, Light Interception, and Photosynthesis in Maize. *Agronomy Journal*, *95*(6), 1465–1474. https://doi.org/10.2134/agronj2003.1465

Sun, Y., Frankenberg, C., Jung, M., Joiner, J., Guanter, L., Köhler, P., & Magney, T. (2018). Overview of Solar-Induced chlorophyll Fluorescence (SIF) from the Orbiting Carbon Observatory-2: Retrieval, cross-mission comparison, and global monitoring for GPP. *Remote Sensing of Environment*, *209*(February), 808–823. https://doi.org/10.1016/j.rse.2018.02.016

Tagliabue, G., Panigada, C., Dechant, B., Baret, F., Cogliati, S., Colombo, R., Migliavacca, M., Rademske, P., Schickling, A., Schüttemeyer, D., Verrelst, J., Rascher, U., Ryu, Y., & Rossini, M. (2019). Exploring the spatial relationship between airborne-derived red and far-red sun-induced fluorescence and process-based GPP estimates in a forest ecosystem. *Remote Sensing of Environment*, *231*(June), 111272. https://doi.org/10.1016/j.rse.2019.111272

Takahashi, Y., Wada, S., Noguchi, K., Miyake, C., Makino, A., & Suzuki, Y. (2021). Photochemistry of Photosystems II and I in Rice Plants Grown under Different N Levels at Normal and High Temperature. *Plant and Cell Physiology*, *0*(February), 1–10. https://doi.org/10.1093/pcp/pcab020

Tsubo, M., Walker, S., & Mukhala, E. (2001). Comparisons of radiation use efficiency of mono-/inter-cropping systems with different row orientations. *Field Crops Research*, *71*(1), 17–29. https://doi.org/10.1016/S0378-4290(01)00142-3

van der Tol, C., Berry, J. A., Campbell, P. K. E., & Rascher, U. (2014). Models of fluorescence and photosynthesis for interpreting measurements of solar-induced chlorophyll fluorescence. *Journal of Geophysical Research: Biogeosciences*, *119*(12), 2312–2327. https://doi.org/10.1002/2014JG002713

Wang, N., Suomalainen, J., Bartholomeus, H., Kooistra, L., Masiliūnas, D., & Clevers, J. G. P. W. (2021). Diurnal variation of sun-induced chlorophyll fluorescence of agricultural crops observed from a point-based spectrometer on a UAV. *International Journal of Applied Earth Observation and Geoinformation*, *96*(December 2020), 102276. https://doi.org/10.1016/j.jag.2020.102276

Wieneke, S., Ahrends, H., Damm, A., Pinto, F., Stadler, A., Rossini, M., & Rascher, U. (2016). Airborne based spectroscopy of red and far-red sun-induced chlorophyll fluorescence: Implications for improved estimates of gross primary productivity. *Remote Sensing of Environment*, *184*, 654–667. https://doi.org/10.1016/j.rse.2016.07.025

Wieneke, S., Burkart, A., Cendrero-Mateo, M. P., Julitta, T., Rossini, M., Schickling, A., Schmidt, M., & Rascher, U. (2018). Linking photosynthesis and sun-induced fluorescence at sub-daily to seasonal scales. *Remote Sensing of Environment*, *219*(October), 247–258. https://doi.org/10.1016/j.rse.2018.10.019

Xu, S., Liu, Z., Zhao, L., Zhao, H., & Ren, S. (2018). Diurnal Response of Sun-Induced Fluorescence and PRI to Water Stress in Maize Using a Near-Surface Remote Sensing Platform. *Remote Sensing*, *10*(10), 1510. https://doi.org/10.3390/rs10101510

Yamori, W., Sakata, N., Suzuki, Y., Shikanai, T., & Makino, A. (2011). Cyclic electron flow around photosystem i via chloroplast NAD(P)H dehydrogenase (NDH) complex performs a

significant physiological role during photosynthesis and plant growth at low temperature in rice. *Plant Journal*, *68*(6), 966–976. https://doi.org/10.1111/j.1365-313X.2011.04747.x

Yang, K., Ryu, Y., Dechant, B., Berry, J. A., Hwang, Y., Jiang, C., Kang, M., Kim, J., Kimm, H., Kornfeld, A., & Yang, X. (2018). Sun-induced chlorophyll fluorescence is more strongly related to absorbed light than to photosynthesis at half-hourly resolution in a rice paddy. *Remote Sensing of Environment*, *216*(July), 658–673. https://doi.org/10.1016/j.rse.2018.07.008

Yang, P., Van Der Tol, C., Campbell, P. K. E., & Middleton, E. M. (2021). Unraveling the physical and physiological basis for the solar-induced chlorophyll fluorescence and photosynthesis relationship using continuous leaf and canopy measurements of a corn crop. *Biogeosciences*, *18*(2), 441–465. https://doi.org/10.5194/bg-18-441-2021

Yang, X., Tang, J., Mustard, J. F., Lee, J. E., Rossini, M., Joiner, J., Munger, J. W., Kornfeld, A., & Richardson, A. D. (2015). Solar-induced chlorophyll fluorescence that correlates with canopy photosynthesis on diurnal and seasonal scales in a temperate deciduous forest. *Geophysical Research Letters*, *42*(8), 2977–2987. https://doi.org/10.1002/2015GL063201

Yin, X., & Struik, P. C. (2012). Mathematical review of the energy transduction stoichiometries of C 4 leaf photosynthesis under limiting light. *Plant, Cell and Environment*, *35*(7), 1299–1312. https://doi.org/10.1111/j.1365-3040.2012.02490.x

Zeng, Y., Badgley, G., Dechant, B., Ryu, Y., Chen, M., & Berry, J. A. (2019). A practical approach for estimating the escape ratio of near-infrared solar-induced chlorophyll fluorescence. *Remote Sensing of Environment*, *232*(April), 111209. https://doi.org/10.1016/j.rse.2019.05.028

Zhang, Q., Zhang, X., Li, Z., Wu, Y., & Zhang, Y. (2019). Comparison of Bi-Hemispherical and Hemispherical-Conical Configurations for In Situ Measurements of Solar-Induced Chlorophyll Fluorescence. *Remote Sensing*, *11*(22), 2642. https://doi.org/10.3390/rs11222642

Zhang, Z., Zhang, Y., Zhang, Q., Chen, J. M., Porcar-Castell, A., Guanter, L., Wu, Y., Zhang, X., Wang, H., Ding, D., & Li, Z. (2020). Assessing bi-directional effects on the diurnal cycle of measured solar-induced chlorophyll fluorescence in crop canopies. *Agricultural and Forest Meteorology*, *295*(April), 108147. https://doi.org/10.1016/j.agrformet.2020.108147

Zhao, F., Dai, X., Verhoef, W., Guo, Y., van der Tol, C., Li, Y., & Huang, Y. (2016). FluorWPS: A Monte Carlo ray-tracing model to compute sun-induced chlorophyll fluorescence of three-dimensional canopy. *Remote Sensing of Environment*, *187*, 385–399. https://doi.org/10.1016/j.rse.2016.10.036

Zhao, F., Gu, X., Verhoef, W., Wang, Q., Yu, T., Liu, Q., Huang, H., Qin, W., Chen, L., & Zhao, H. (2010). A spectral directional reflectance model of row crops. *Remote Sensing of Environment*, *114*(2), 265–285. https://doi.org/10.1016/j.rse.2009.09.018

Zhao, F., Li, Y., Dai, X., Verhoef, W., Guo, Y., Shang, H., Gu, X., Huang, Y., Yu, T., & Huang, J. (2015). Simulated impact of sensor field of view and distance on field measurements of bidirectional reflectance factors for row crops. *Remote Sensing of Environment*, *156*, 129–142. https://doi.org/10.1016/j.rse.2014.09.011

List of Figure Captions

Figure 1. Diurnal dynamics of SIF measured over CMRF. a) SIF_{760} retrieved from the FAME-1 tower during clear days at peak growing season from the FAME-1 tower. b) SIF_{760} retrieved from the FAME-1 UAV flown over two corn fields at CMRF with north-south (N-S) or east-west (E-W) row orientation. Here, SIF is retrieved using SFM_{narrow} (759.5-761.5 nm). For a), markers indicate half-hour average of all clear sky measurements recorded over 2019 from peak growing season (DOY 200 to DOY 250). For b), markers represent average for 6 plots for N-S field or 5 plots for E-W field measured in 2019. Error bars in both panels indicate one standard deviation. Dashed vertical lines indicate average solar noon for this location.

Figure 2. Absorbed photosynthetically active radiation (APAR, top row) and fraction of absorbed photosynthetically active radiation (fPAR, bottom row) at (a,c) CMRF and (b,d) MOFLUX sites on clear-sky conditions. Data shown for panels (a,c) were measured concurrently with 2019 SIF measurements presented in Fig. 1a. The corn field measured by the tower at CMRF has N-S row orientation. Points indicate half-hourly average of instantaneous measurements for CMRF and MOFLUX. Error bars in all panels indicate one standard deviation.

Figure 3. Diurnal patterns of a) canopy escape probability (ε), b) near-infrared radiance of vegetation (NIR_V), c) normalized difference vegetation index (NDVI) and near-infrared reflectance (ρ_{NIR}) recorded by FAME-1 over a N-S oriented corn field at CMRF. Measurements indicate average (black line) and one standard deviation (gray shading) recorded by FAME-1 over five clear days of the peak growing season in 2019.

Figure 4. Energy partitioning in top of canopy and mid-canopy leaves of corn planted in (a,b) N-S or (c,d) E-W row orientation. Measurements were taken at CMRF on DOY 236 in 2018 (for N-S) and DOY 217 in 2019 (E-W). Lines indicate average of 5-6 leaves at the top (a,c) or mid canopy (b,d) position in each field. Panel insets highlight the diurnal patterns of Φ_F.

Figure 5. qL, NPQ, and Φ_F generated for eight canopy layers from top (LAI = 0) to bottom of the canopy. Total canopy LAI is assumed to be 4 for simulation purposes. The simulation approach is described in section 2.4.3. Each layer represents a canopy optical depth of LAI = 0.5, e.g., the legend "LAI = 0" represents the layer from top of the canopy (i.e., LAI = 0) to LAI = 0.5.

Figure 6. Diurnal pattern of measured SIF_{760} contrasted with SIF_{760} retrieved using SFM_{narrow}, simulated using three combinations of structure and physiology factors. The function shown above each panel indicates which actual measurements were included in the simulation; factors not shown in the function were held constant. R^2 value is shown for correlation between simulated and measured SIF.

Figure 7. Diurnal SIF dynamics retrieved using traditional and adjusted SFM fitting windows by bi-hemispherical (FAME) and hemispherical-conical (FloX) system configurations. (a) Measurements collected by FAME-1 over a corn field; points indicate average of 3-6 clear days per year recorded over 2018-2019 from peak growing season. (b) Measurements obtained by FAME-2 over a deciduous forest; points indicate average of 11 clear days during May-June of 2017. (c) Measurements obtained by FloX-1 over a site consisting of alfalfa and forage; points indicate average of 8 clear days recorded over April-June of 2018. (d) Measurements obtained by FloX-2 over a grass site; points indicate average of 12 clear days recorded over April-May of 2018. The dashed vertical lines indicate the average time of solar noon across all clear days; error bars indicate standard deviation. Red markers denote SIF

retrieved using the wide fitting window (759-767.76 nm); blue markers denote SIF retrieved using the adjusted narrow fitting window (759.5-761.5 nm for FAME, 758-764 nm for FloX). Note that the y-axes have different scaling.

Figure 8. Illustration of potential for over- or under-estimation of SIF using a daily integral of the cosine of the solar zenith angle. Colored points represent different satellite overpass times (9:00, 12:00, 13:30 h). Colored dashed lines indicate SIF extrapolated from each point using the cosine of the solar zenith angle. The black line is a representation of a "true" SIF signal in a N-S oriented agricultural field, such as observed in our study.